

ICRF modelling in 2D & 3D magnetic configurations using a hot plasma model

M Machielsen, J P Graves, W A Cooper

Ecole Polytechnique Fédérale de Lausanne (EPFL), Swiss Plasma Center (SPC),
CH-1015 Lausanne, Switzerland

E-mail: mike.machielsen@epfl.ch

June 2021

Abstract. The generation of energetic trapped ions is important for experiments investigating their confinement in 3D magnetic fields, for plasma heating, for studies into unwanted drive of instabilities, and improved transport regimes. An effective way to generate such energetic ions is with ion cyclotron resonance heating. SCENIC is a tool built to self consistently model the magnetic equilibrium, the radio frequency wave, and the minority distribution function in steady state. In this paper the impact of higher order finite Larmor radius corrections in the dielectric tensor will be described. The RF electric field and the power deposition in the new hot model are compared against the previously used warm model for several JET plasmas. Considerable differences are found in some of the scenarios. The new version of the wave code LEMan also supports the direct use of particle-in-cell marker data to compute the dielectric tensor. An expression for the dielectric tensor is derived, and it is applied to a test case in JET. The power deposition profile agrees very well with that of a Maxwellian reference case, which is promising for future applications. Moreover, a full SCENIC run shows a significantly enhanced fast ion tail. In a demonstration of the novel features of LEMan, it is also applied to minority heating in the intrinsically 3D plasma of W7-X.

Keywords: ICRF, ion cyclotron heating, hot plasma, stellarator, Wendelstein 7-X, fast ion confinement, anisotropy

1. Introduction

Radio waves in the ion cyclotron range of frequencies (ICRF) are used routinely for heating, suppressing sawteeth, preventing impurity accumulation and driving current in fusion plasmas. Moreover, ICRF is known to generate long tails in the distribution function of resonant ions, see e.g. Refs. [1, 2, 3, 4]. These fast ion tails often have a large temperature anisotropy T_{\perp}/T_{\parallel} , which affects the RF power deposition, and also the magnetic equilibrium [5, 6]. In addition, plasmas with significant radio wave heating

can also increase the fusion reaction rate [7, 8].

Accurate modelling of ICRF heating is therefore important for designing experiments, explaining experimental findings, and extrapolating to future fusion reactors. Early models started out with a cold plasma description, which can model wave propagation but fails at describing RF power deposition. The wave damping has to be included ad hoc. One step higher in complexity is to include a non-zero thermal motion parallel to the background magnetic field. This “smooths” out the singularity in the dielectric tensor at the cyclotron resonance, and replaces this contribution with the plasma dispersion function. The approach is able to describe Landau and fundamental cyclotron resonance but it still neglects corrections due to finite Larmor radius (FLR) effects, which can contribute considerably to the wave propagation and absorption depending on the heating scheme. These effects include e.g. higher harmonic heating, electron transit time magnetic pumping (eTTMP) and the damping of the right handed polarised fast wave by fast ions. Inclusion of such effects requires at least a first order warm plasma description. In this paper a plasma model will be referred to as “warm” if a truncated expansion in FLR parameter is used, “hot” is reserved for models without truncation.

In addition, it is important to model the RF wave self consistently with the distribution function of the resonant species, which is often non-Maxwellian. The evolution of this distribution depends on the RF electric field, which itself depends on the distribution through the dielectric tensor. Modelling the simultaneous time evolution of both quantities is not feasible with current computational resources because the time scale for the wave to propagate throughout the system is orders of magnitude smaller than the collisional time scale, which is the time required for the distribution function to change considerably. However, the main interest is not time evolution itself, but the equilibrium distribution and the corresponding electric field. This final state can be obtained much more efficiently by iteratively solving for the RF electric field and the distribution function. This approach has been adopted by coupling RF codes to Fokker-Planck/Monte Carlo codes, e.g. SELFO [9], AORSA-CQL3D [10], CYRANO-BATCH [11], TORIC-SSFPQL [12] and SCENIC [13], see table 1.

The focus of the present paper is to describe how the LEMan code (part of SCENIC) has been upgraded to model collisionless damping near arbitrary cyclotron harmonics for a selection of different minority distribution functions. Recently, a hot plasma description has been explored by LEMan for a Maxwellian distribution in Ref. [14]. But of particular interest is the modified Bi-Maxwellian from Ref. [15]. Unlike a regular Bi-Maxwellian, this analytic distribution satisfies the Fokker-Planck equation to lowest order and it models the effect of the concentration of bounce points along the line of resonance. This form of Bi-Maxwellian has been implemented in the full SCENIC package for ICRH modelling. Recently, this distribution has also been used in Ref. [16]

for a study on tungsten accumulation using SCENIC. An integral form of the dielectric tensor is presented, which is suitable for numerical evaluation. Instead of using a general numerical velocity space integral, this form is optimised for the modified Bi-Maxwellian. Its implementation in LEMan is compared against several other dielectric tensor models. In addition an analytic expression for a dielectric tensor is derived that can use particle in cell (PIC) data directly. Example cases in JET for both of these dielectric tensors are included.

Note that formally the plasma response is an integral operator in configuration space. However, to make it more tractable this has been simplified considerably in LEMan by assuming that locally a single wave vector dominates. This replaces the integral operator by a matrix that represents the conductivity tensor. It is therefore relatively easy to adopt a description valid to all orders in Larmor radius because the rest of the code is independent of how the matrix is computed. However, this limits the description to scenarios where the fast wave is by far the dominant mode. Therefore LEMan cannot be applied to scenarios where mode conversion plays a considerable role. However, the strength of LEMan is its ability to model 3D geometries such as tokamaks with a kink mode perturbation and stellarators, which need not be stellarator-symmetric (analogous to up-down asymmetry in tokamaks). In addition, LEMan is integrated into the SCENIC code package (comprised of ANIMEC [17], LEMan and VENUS-LEVIS [18]), which allows a self consistent computation of the magnetic equilibrium, the RF wave field, and the minority distribution function. This is not the first coupled code package, many others have been developed over the years, with varying levels of model reduction, see table 1. A common reduction in the Fokker-Planck/Monte-Carlo codes is to average the particle orbits over a bounce period. The evolution of the minority distribution function in SCENIC is done with VENUS-LEVIS, which is a 4D (or 6D) orbit tracing code, without any type of bounce averaging, see Section 5.1. It thus includes finite orbit width (FOW) effects, which are known to broaden the collisional power deposition profile. Additionally, FOW effects also lead to increased particle losses, especially in the high energy range [19].

The paper is organised as follows: In Section 2 the basic equations will be presented and two new dielectric tensors will be derived. This derivation is valid to all orders in Larmor radius, and to arbitrary order in cyclotron harmonic. In Section 3 a comparison will be made between a warm plasma model and the newly implemented hot model for various heating schemes and distribution functions in JET. Several heating schemes will be examined in more detail. In Section 4 the PIC dielectric tensor will be compared against a reference case in JET. After that a full SCENIC run will be performed for a selected JET case in Section 5. A simulation of minority heating in the W7-X stellarator will be presented in Section 6. Lastly, concluding and summarising comments are reserved for Section 7.

Table 1: Summary of several coupled 2D & 3D ICRF full-wave codes, not an exhaustive list. MC = mode conversion, FEM = finite element method.

RF Code	Numerical Approach		Geometry	FLR effects	MC	Coupled to
AORSA [20]	Fourier method	collocation	tokamak/stellara-tor	All orders	Yes	CQL3D [10]
TORIC [21, 22]	radial FEM, toroidal and poloidal modes		tokamak	truncated	Yes	SSFPQL [12]
EVE [23]	radial FEM, toroidal and poloidal modes		tokamak	truncated	Yes	SPOT[24]
CYRANO [25, 26]	radial FEM, toroidal and poloidal modes		tokamak	truncated	Yes	BATCH [27]
LION [28]	radial and poloidal FEM, toroidal modes		tokamak	All orders	No	FIDO (SELFO [9, 29])
LEMan	radial FEM, toroidal and poloidal modes		tokamak/stellara-tor	All orders	No	VENUS-LEVIS (SCENIC)

2. The dielectric tensor

Required for the calculation of wave propagation and damping is the dielectric tensor, which encodes the properties of the plasma and magnetic equilibrium. This section serves to derive it.

2.1. The wave equation

Starting from Maxwell's equations, the magnetic field can be eliminated by combining Faraday and Ampere's law,

$$\nabla \times (\nabla \times \mathbf{E}_1(\mathbf{r}, t)) + \frac{1}{c^2} \frac{\partial \mathbf{E}_1(\mathbf{r}, t)}{\partial t} = -\mu_0 \frac{\partial \mathbf{J}_1(\mathbf{r}, t)}{\partial t} \quad (1)$$

with \mathbf{E}_1 the RF electric field, \mathbf{J}_1 the associated current density, \mathbf{r} the position, c the speed of light, t time, and μ_0 the vacuum permeability. In the frequency domain this wave equation transforms into a Helmholtz type equation,

$$\nabla \times (\nabla \times \hat{\mathbf{E}}_1) - \frac{\omega^2}{c^2} \hat{\mathbf{E}}_1 = i\omega\mu_0 \hat{\mathbf{J}}_1 = i\omega\mu_0 (\hat{\mathbf{J}}_{ant} + \hat{\mathbf{J}}_p) \quad (2)$$

with ω the angular frequency \ddagger , $\hat{\mathbf{J}}_{ant}$ the antenna current, and $\hat{\mathbf{J}}_p$ the induced plasma current (also called plasma response). The hat indicates the quantities are in the frequency domain. The challenge is computing the electric field and the plasma current self consistently. In order to proceed a constitutive relation will be used, i.e. a relation of the type $\hat{\mathbf{J}}_p = \hat{\mathbf{J}}_p(\mathbf{E}_1)$.

On the time scale of the wave $1/\omega$ the effect of particle collisions, sources and sinks on the distribution function may be neglected. Thus it is sufficient to use the Vlasov equation. Furthermore, as is typical in the ICRF literature, the wave amplitude is assumed to be small, and hence the Vlasov equation can be linearised. Integration along the unperturbed paths yields the first order correction to the distribution function f_1 .

$$f_1(\mathbf{r}, \mathbf{v}, t) = -\frac{q}{m} \int_{-\infty}^t dt' [\mathbf{E}_1(\mathbf{r}', t') + \mathbf{v}' \times \mathbf{B}_1(\mathbf{r}', t')] \cdot \nabla_{\mathbf{v}'} f_0(\mathbf{r}', \mathbf{v}', t') \quad (3)$$

With q the particle charge, m the mass, \mathbf{v} the velocity, \mathbf{B}_1 the RF magnetic field and f_0 the background distribution function. The primed quantities describe a path in phase space, unperturbed by the RF field, ending in $(\mathbf{r}, \mathbf{v}, t)$. The first moment of f_1 yields the perturbed current density,

$$\mathbf{J}_p(\mathbf{r}, t) = q \int_{\mathbb{R}^3} d^3v \mathbf{v} f_1(\mathbf{r}, \mathbf{v}, t), \quad (4)$$

which is a linear function of the electric field under these assumptions. From this constitutive relation the conductivity tensor (and thus the dielectric tensor as well) can then be derived. A comprehensive explanation of this topic can be found in e.g. [30, 31, 32]. So the Helmholtz equation can be written as

$$\nabla \times (\nabla \times \hat{\mathbf{E}}_1(\mathbf{r})) - \frac{\omega^2}{c^2} \hat{\mathbf{E}}_1(\mathbf{r}) - i\omega\mu_0 \int_{\mathbb{R}^3} d^3r' \hat{\boldsymbol{\sigma}}(\mathbf{r}, \mathbf{r} - \mathbf{r}') \cdot \hat{\mathbf{E}}_1(\mathbf{r}') = i\omega\mu_0 \hat{\mathbf{J}}_{ant}(\mathbf{r}), \quad (5)$$

an integro-differential equation, with conductivity kernel $\hat{\boldsymbol{\sigma}}(\mathbf{r}, \mathbf{r} - \mathbf{r}')$. The integral operator indicates that the problem is non-local. In other words, to compute the plasma response $\hat{\mathbf{J}}_p(\mathbf{r}_0)$ at some point \mathbf{r}_0 the electric field is required not just at \mathbf{r}_0 (and/or an infinitesimal distance away) but also at a finite distance from \mathbf{r}_0 . In a uniform plasma this operator simplifies to a convolution, however, in the inhomogeneous case two arguments are required for the kernel: the first is the position for evaluating the magnetic field and plasma parameters, the second represents the distance with respect to this reference point. In cold plasma the elements of the conductivity kernel are proportional to a delta function, thus reducing to a local equation. This does not happen in warm and hot plasma models because the kernel has a finite width. However, a pragmatic approach is to bluntly assume that locally at each point a single wave vector

\ddagger In the common scenario of monochromatic heating, i.e. a single antenna frequency ω_{ant} , no frequencies other than $\omega = \omega_{ant}$ need to be considered because the Helmholtz equation is linear.

$\mathbf{k}_{eff}(\mathbf{r})$ dominates,

$$\begin{aligned}\hat{\mathbf{J}}_p(\mathbf{r}) &= \int_{\mathbb{R}^3} d^3r' \left[\left(\frac{1}{2\pi} \right)^3 \int_{\mathbb{R}^3} d^3k \check{\boldsymbol{\sigma}}(\mathbf{r}, \mathbf{k}) e^{i\mathbf{k} \cdot (\mathbf{r} - \mathbf{r}')} \right] \cdot \hat{\mathbf{E}}_1(\mathbf{r}') \\ &\approx \int_{\mathbb{R}^3} d^3r' \left[\left(\frac{1}{2\pi} \right)^3 \int_{\mathbb{R}^3} d^3k \check{\boldsymbol{\sigma}}(\mathbf{r}, \mathbf{k}_{eff}(\mathbf{r})) e^{i\mathbf{k} \cdot (\mathbf{r} - \mathbf{r}')} \right] \cdot \hat{\mathbf{E}}_1(\mathbf{r}') \\ &= \check{\boldsymbol{\sigma}}(\mathbf{r}, \mathbf{k}_{eff}(\mathbf{r})) \cdot \hat{\mathbf{E}}_1(\mathbf{r}).\end{aligned}\tag{6}$$

This effective wave vector \mathbf{k}_{eff} is computed self consistently from the gradient of the scalar potential, see Appendix B of Ref. [13]. The Helmholtz equation is therefore written as

$$\nabla \times (\nabla \times \hat{\mathbf{E}}_1(\mathbf{r})) - \frac{\omega^2}{c^2} \check{\mathbf{K}}(\mathbf{r}, \mathbf{k}_0(\mathbf{r})) \cdot \hat{\mathbf{E}}_1(\mathbf{r}) = i\omega\mu_0 \hat{\mathbf{J}}_{ant}(\mathbf{r}),\tag{7}$$

where the dielectric tensor is defined in terms of the conductivity tensor as

$$\check{\mathbf{K}} = \mathbf{I} + \frac{i\check{\boldsymbol{\sigma}}}{\omega\varepsilon_0},\tag{8}$$

with ε_0 the vacuum permittivity. The approximate solution to Eq. (7) does not automatically guarantee $\nabla \cdot \mathbf{B}_1 = 0$, which can lead to spurious solutions [33]. One way to deal with this is by casting the Helmholtz equation in potential formulation [34, 35, 36]. This is the approach taken by LEMan, which is free of numerical pollution, given that the gauge condition is satisfied. The Coulomb gauge is used, which results in

$$\begin{aligned}\nabla^2 \hat{\mathbf{A}} + \frac{\omega^2}{c^2} \check{\mathbf{K}} \cdot \hat{\mathbf{A}} + \frac{i\omega}{c^2} \check{\mathbf{K}} \cdot \nabla \hat{\chi} &= -\mu_0 \hat{\mathbf{J}}_{ant} \\ \nabla \cdot (\check{\mathbf{K}} \cdot \nabla \hat{\chi}) - i\omega \nabla \cdot (\check{\mathbf{K}} \cdot \hat{\mathbf{A}}) &= -\hat{\rho}_{ant}/\varepsilon_0\end{aligned}\tag{9}$$

with $\hat{\chi}$ the scalar potential, $\hat{\mathbf{A}}$ the vector potential and $\hat{\rho}_{ant}$ the antenna charge density. The second line can be obtained from the divergence of the first, and using charge conservation. Since LEMan adopts a divergence free antenna current $\hat{\rho}_{ant} = 0$. Eq. (9) is solved in the weak form using a finite element method in radial direction, and a Fourier series approach for the two angular directions [36]. In the general case LEMan solves for the full 3D problem in one simulation. However, in axisymmetric devices the different toroidal modes of the wave field are decoupled, which allows for a significant optimisation: The full 3D problem with a total of N_{tor} toroidal modes can be split up into N_{tor} independent 2D simulations. Due to interference the actual wave field is still 3D, but this field can be reconstructed by summing together all N_{tor} toroidal modes at the end.

2.2. Derivation of dielectric tensor for modified Bi-Maxwellian

In order to derive the dielectric tensor, the background distribution function f_0 needs to be known, for each species. A “regular”, non-drifting, Bi-Maxwellian can be defined

as follows:

$$f_0(s, v_{\parallel}, v_{\perp}) = \frac{N(s)}{\pi^{3/2} v_{T_{\parallel}}(s) v_{T_{\perp}}^2(s)} \exp \left[- \left(\frac{v_{\parallel}^2}{v_{T_{\parallel}}^2(s)} + \frac{v_{\perp}^2}{v_{T_{\perp}}^2(s)} \right) \right], \quad (10)$$

with thermal velocities

$$v_{T_{\perp}} = \sqrt{2T_{\perp}/m} \geq 0, \quad v_{T_{\parallel}} = \sqrt{2T_{\parallel}/m} \geq 0. \quad (11)$$

Here N is the density, T_{\parallel} the parallel temperature, T_{\perp} the perpendicular temperature and s the radial flux surface label (normalised toroidal flux). However, in order to satisfy the Fokker-Planck equation to lowest order, a distribution function must have $\mathbf{B} \cdot \nabla f_0 = 0$, where \mathbf{B} is the background magnetic field. One particular Bi-Maxwellian that satisfies this constraint is given by Eq. (12) below [15, 37, 17]. Earlier simulations show that ICRH can result in poloidal density variation of the heated minority species. It can also form lobes along the trapped-passing boundary in $(v_{\parallel}, v_{\perp})$ space [38, 39, 40], see figure 1 for an example. Contrary to a regular Bi-Maxwellian, this distribution is able to capture such effects. In addition, it explicitly contains the dependency on the magnetic field strength B_C , the approximate field where the wave-particle resonance applies, while still being analytically tractable,

$$f_0(s, E, \mu) = \frac{\mathcal{N}(s)}{\pi^{3/2} v_{T_{\perp}}^3(s)} \exp \left[- \left(\frac{\mu B_C}{T_{\perp}(s)} + \frac{|E - \mu B_C|}{T_{\parallel}(s)} \right) \right], \quad (12)$$

with the magnetic moment $\mu = mv_{\perp}^2/(2B)$, energy $E = mv^2/2$. The critical field B_C can in principle depend on s , but is here chosen as a constant. In the context of ICRF, this critical field indicates the wave-particle resonance (without Doppler shift) of a chosen species, i.e. where $\omega = n\Omega$ is satisfied. This relates the antenna frequency ω to the critical field through $B_C = \frac{m\omega}{n|q|}$, with Ω, n , the cyclotron frequency and cyclotron harmonic of a species of choice respectively. The variable $\mathcal{N}(s)$ in Eq. (12) is the density factor, integrating (12) over velocity space gives the “true” density [37]:

$$N(s, B) = \mathcal{N}(s) \sqrt{\frac{T_{\parallel}}{T_{\perp}}} \mathcal{C}(s, B) \quad (13)$$

$$\mathcal{C}(s, B) = \begin{cases} \frac{B/B_C}{1 - (T_{\perp}/T_{\parallel})(1 - B/B_C)} & B \geq B_C \\ \frac{B}{B_C} \frac{1 + (T_{\perp}/T_{\parallel})(1 - B/B_C) - 2(T_{\perp}/T_{\parallel})^{3/2}(1 - B/B_C)^{3/2}}{1 - (T_{\perp}/T_{\parallel})^2(1 - B/B_C)^2} & B < B_C. \end{cases} \quad (14)$$

Note, the true density N is not solely a flux surface variable for this distribution, i.e. there is a B dependence which in turn varies with position (s, θ, φ) . This feature of anisotropy is because trapped particles that intersect the resonant surface ($B = B_C$) tend to align their bounce tips with this layer. Hence the distribution function becomes distorted over the poloidal cross section. The flux surface averaged density is

$$\langle N \rangle = \mathcal{N} \sqrt{\frac{T_{\parallel}}{T_{\perp}}} \langle \mathcal{C} \rangle \approx \mathcal{N} \sqrt{\frac{T_{\parallel}}{T_{\perp}}} = N(s, B_C) \quad (15)$$

with the averaging operator denoted by angle brackets $\langle \rangle$.

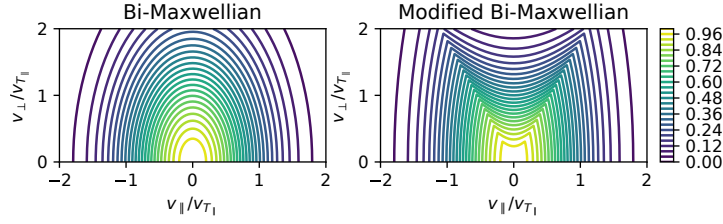


Figure 1: Comparison of the regular and modified Bi-Maxwellian distributions. Contour plot of $f_0(s, v_{\parallel}, v_{\perp})/f_0(s, 0, 0)$, for $B_C/B = 1.3$ and $T_{\perp}/T_{\parallel} = 3$. The contours of the regular Bi-Maxwellian form ellipses, while those of the modified distribution only do so on the high field side.

Analytic expressions for the dielectric tensor for (drifting) Maxwellian or Bi-Maxwellian distributions are well established. See for instance Ref. [32] for a derivation. However, no such expression has been derived for the modified Bi-Maxwellian, Eq. (12). The required integrals for a general $f_0(v_{\parallel}, v_{\perp})$ are given by Eqs. 4.184-4.191 in Ref. [32]. The velocity space integration is over $v_{\perp} \in [0, \infty)$, $v_{\parallel} \in (-\infty, \infty)$. On the HFS ($B \geq B_C$), $E - \mu B_C \geq 0$ always, and thus the absolute value bars can be removed from Eq. (12). The dielectric tensor for Eq. (12) can then be found using substitution into the known Bi-Maxwellian case, see Eq. (A.4). However, removing the absolute value bars on the LFS ($B < B_C$) would split the velocity space integral in two pieces. No analytic expression for this integral was found. The objective therefore has been to cast the integrals in a form which can be computed numerically with double precision floats. On the LFS the contribution of the fast ion species to the dielectric tensor element l can be cast into the following form:

$$\begin{aligned}
 K_l &= \Upsilon_l \sum_{n=-\infty}^{\infty} \varsigma_{l,n} \int_{\gamma} \left(p_{l,0} M_{h_l}(x) + p_{l,1} N_{h_l}(x) + \frac{q_{l,0} M_{h_l}(x) + q_{l,1} N_{h_l}(x)}{x - \xi_n} \right) dx \\
 &= \Upsilon_l \sum_{n=-\infty}^{\infty} \varsigma_{l,n} (p_{l,0} \Gamma_{h_l} + p_{l,1} \Delta_{h_l} + q_{l,0} \Phi_{h_l}(\xi_n) + q_{l,1} \Psi_{h_l}(\xi_n))
 \end{aligned} \tag{16}$$

with $l \in \{0, 1, 2, 3, 4, 5, 6, 7\}$. The functions M_{h_l}, N_{h_l} represent integrals over the perpendicular velocity. The integration over the parallel velocity is done along the path γ , which goes along the real axis, making an excursion below the pole. The auxiliary functions are defined as follows:

$$\begin{aligned}
 \Gamma_h &= \int_{-\infty}^{\infty} M_h(x) dx = 2 \int_0^{\infty} M_h(x) dx \\
 \Delta_h &= \int_{-\infty}^{\infty} N_h(x) dx = 2 \int_0^{\infty} N_h(x) dx \\
 \Phi_h(\xi_n) &= \int_{\gamma} \frac{M_h(x)}{x - \xi_n} dx \\
 \Psi_h(\xi_n) &= \int_{\gamma} \frac{N_h(x)}{x - \xi_n} dx
 \end{aligned} \tag{17}$$

See Appendix A.2 for the definitions of the additional variables and functions. Computing Φ, Ψ by naively sampling the integrand closer and closer to the singularity will not work as the values blow up there. Instead, using a series expansion to high order was also considered, but this led to insurmountable cancellation errors. Notice that the functions Φ_h, Ψ_h in (17) are Hilbert transforms. Libraries exist for numerically computing the Hilbert transform. A popular method is transforming to the Fourier domain to get rid of the convolution and transforming back after the multiplication. However, in this work just one point is required, not a whole spectrum. Fortunately, transforming to the Fourier domain is not necessary, since the singularity is a removable one. Meaning that the function is bounded in the neighbourhood of the singularity, and the value at the singularity can be replaced by its limiting value. In order to see this, the integral must be rewritten, e.g. for Φ_h this process is shown in Eq. (18): The integral over x is first split into a principle value plus a residue, then $M_h(\xi_n)$ is both added and subtracted in the numerator. The integral over $(x - \xi_n)^{-1}$ drops out[§] due to symmetry, and what is left does no longer blow up near the singularity.

$$\begin{aligned}
\Phi_h(\xi_n) &= \int_{\gamma} \frac{M_h(x)}{x - \xi_n} dx = PV \int_{-\infty}^{\infty} \frac{M_h(x)}{x - \xi_n} dx + \pi i M(\xi_n) \\
&= PV \int_{-\infty}^{\infty} \frac{M_h(x) - M_h(\xi_n)}{x - \xi_n} dx + M_h(\xi_n) PV \int_{-\infty}^{\infty} \frac{1}{x - \xi_n} dx + \pi i M_h(\xi_n) \quad (18) \\
&= 2\xi_n PV \int_0^{\infty} \frac{M_h(x) - M_h(\xi_n)}{x^2 - (\xi_n)^2} dx + \pi i M_h(\xi_n)
\end{aligned}$$

The integral can now be approximated with standard quadrature methods, which is well within the realm of modern CPU capabilities, even on a 3D grid. In this work the composite Simpson's rule is used, for non-uniform grids. The integration limits can be truncated as for large x, y the integrand becomes negligible. An infinite sum over the cyclotron harmonic n remains, which in practice has to be truncated. The maximum value of n can be set by the user of LEMan. However, RF heating scenarios rarely involve harmonics above $n = 3$. So the series can be truncated rather quickly. Lastly, note that it can be shown that for the modified Bi-Maxwellian $K_6 = K_4, K_7 = K_5$.

2.3. PIC dielectric tensor

2.3.1. Background distribution function The expression for the dielectric tensor may be extended to include a parallel velocity asymmetry (parallel drift velocity), which is useful for beam populations. However, the parallel velocity will not be uniform on a flux surface, due to varying pitch angles of ions ionised at a different major radii. There may be other complicated effects in addition to this that distort the distribution function. Therefore it may be useful not to assume any analytic distribution. Instead the marker

[§] Sidenote: for this ξ_n needs to be real. However, this was already assumed. If $\text{Im}(\xi_n) \neq 0$ the original integral could already be integrated directly as $x \in \mathbb{R}$ thus there is no singularity. So if $\xi_n \in \mathbb{R}$, after change of variables the integrand is odd.

information coming from a particle-in-cell model can be used directly. This avoids the potential quality loss during fitting. Such a PIC distribution will be of the form

$$f_0(\mathbf{r}, v_{\parallel}, v_{\perp}, \phi) = \sum_k w_k \delta(\mathbf{r} - \mathbf{r}_k) \delta(v_{\parallel} - v_{\parallel,k}) \frac{\delta(v_{\perp} - v_{\perp,k})}{v_{\perp}} \delta(\phi - \phi_k), \quad (19)$$

with ϕ the gyro angle and w_k the weight of a marker k . Notice the $1/v_{\perp}$ that appears in Eq. (19), which is due to the Jacobian in cylindrical coordinates. I.e. this ensures $\int_{\mathbb{R}^3} \delta(\mathbf{v} - \mathbf{v}_j) d^3v = 1$. What follows next is a series of successive simplifications of Eq. (19) to make it more tractable. The main interest is not in the microscopic electromagnetic fields created by these markers. The fine structure below the Debye length scale is unimportant. Instead the macroscopic (averaged) fields are of interest. So it makes sense to introduce some smoothing. Averaging over a volume $V(\mathbf{r})$ around \mathbf{r} gives:

$$f_0(\mathbf{r}, v_{\parallel}, v_{\perp}, \phi) = \frac{1}{V(\mathbf{r})} \sum_j w_j \delta(v_{\parallel} - v_{\parallel,j}) \frac{\delta(v_{\perp} - v_{\perp,j})}{v_{\perp}} \delta(\phi - \phi_j) \quad (20)$$

where \sum_j is now solely over the markers j within this volume. The choice of averaging volume will be discussed in Section 2.3.2. Furthermore, the shape function $\delta(v_{\parallel} - v_{\parallel,j})$ can be replaced by an exponential, preserving the norm. The next step is averaging over the gyro angle,

$$f_0(\mathbf{r}, v_{\parallel}, v_{\perp}) = \frac{1}{V(\mathbf{r})} \sum_j w_j \frac{1}{\sqrt{\pi}\sigma_j} \exp \left[- \left(\frac{v_{\parallel} - v_{\parallel,j}}{\sigma_j} \right)^2 \right] \frac{\delta(v_{\perp} - v_{\perp,j})}{v_{\perp}} \frac{1}{2\pi}. \quad (21)$$

The standard deviation of this exponential is $\sigma_j/\sqrt{2}$, and it should be chosen such that $\sigma_j \ll \sqrt{2}v_{T_{\parallel}}$, but not so small that the distribution function would become too noisy (too many markers required). The subscript j is added to σ_j , since in general σ_j could be marker dependent. The weights sum up to the total number of particles within that volume, $N(\mathbf{r})V(\mathbf{r}) = \sum_j w_j$, giving

$$f_0(\mathbf{r}, v_{\parallel}, v_{\perp}) = \frac{N(\mathbf{r})}{2\pi \sum_j w_j} \sum_j w_j \frac{1}{\sqrt{\pi}\sigma_j} \exp \left[- \left(\frac{v_{\parallel} - v_{\parallel,j}}{\sigma_j} \right)^2 \right] \frac{\delta(v_{\perp} - v_{\perp,j})}{v_{\perp}}. \quad (22)$$

2.3.2. Choice of averaging volume In order to compute the dielectric tensor in some point \mathbf{r}_0 , the average distribution $f_0(\mathbf{r}_0, v_{\parallel}, v_{\perp})$ is required and therefore an averaging volume needs to be selected. The volume $V(\mathbf{r}_0)$ which contains \mathbf{r}_0 should be chosen as large as possible to improve statistics, but without destroying nuanced features of the distribution. The choice therefore depends strongly on the scenario, several examples are shown in figure 2.

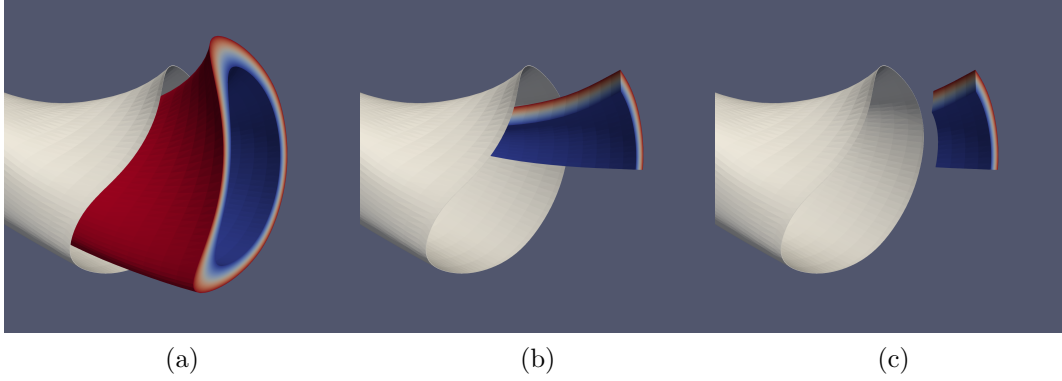


Figure 2: Three choices of averaging volume for W7-X. In white the LCFS, in colour the volume V , with blue indicating the radial inside, and red the radial outside. From left to right: a full flux tube, a filament, and a section of a filament. The size of the volume has been exaggerated in order to see it more clearly, so not to scale.

Clearly, the variation of f_0 is strong in radial direction, and therefore the radial extension needs to be limited, figure 2a. This is the volume between two flux surfaces, with \mathbf{r}_0 lying on the central flux surface. Note, this still has the full 2π poloidal and toroidal extension, thus inherent differences between the LFS and HFS are averaged over. Therefore, this is not compatible with the modified Bi-Maxwellian distribution, Eq. (12), because the density is not a flux function. One level more accurate would be the filament (flux tube segment) in figure 2b. This is able to distinguish between differences in the LFS and HFS. Depending on the distribution this too can be inadequate, e.g. for cases with heating or fuelling that is not uniformly distributed in toroidal angle, combined with significant toroidal trapping. In this case the volume has to be reduced even further, as depicted in figure 2c.

Increasing the number of grid points ($\mathbf{r}_0, \mathbf{r}_1, \mathbf{r}_2, \dots$) does not mean that the volumes shrink, that is because they are allowed to overlap, see figure 3. The volume type and size is chosen based on physical arguments and available marker count, not the grid resolution.

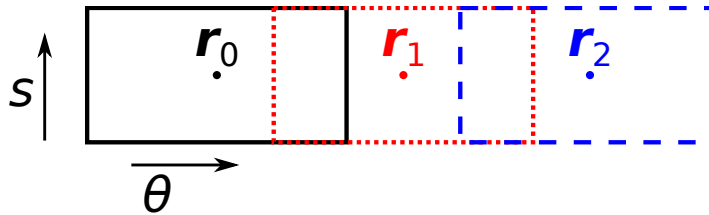


Figure 3: Cartoon showing three grid points, with their associated averaging volumes (filament type), in the poloidal plane.

2.3.3. Computing the dielectric tensor The dielectric tensor elements can now be computed, using Eqs. (4.184-4.191) of Ref. [32]. The following integrals will be

necessary:

$$\int_0^\infty g(x)\delta'(x-x_0)dx = -g'(x_0), \quad \text{where } x_0 > 0 \quad (23)$$

which is obtained by integration by parts. Secondly,

$$\frac{1}{\sqrt{\pi}} \int_{-\infty}^\infty \frac{xe^{-x^2}}{x-z}dx = -\frac{1}{2}Z'(z) = 1 + zZ(z) \quad (24)$$

where Z is the plasma dispersion function defined in Eq. (A.5). In addition, higher powers in the numerator of the integrand can be rewritten to obtains terms with Z or Z' , e.g.:

$$\frac{x^2}{x-z} = \frac{x(x-z) + zx}{x-z} = x + \frac{zx}{x-z}, \quad (25)$$

where the x drops out from the integration as it is odd. Lastly, the second derivative of the Bessel function can be eliminated from the Bessel equation itself,

$$z^2 J_n''(z) + zJ_n'(z) + (z^2 - n^2)J_n(z) = 0. \quad (26)$$

Using the above, the dielectric tensor elements can be written as

$$\begin{aligned} K_l &= \frac{\omega_p^2/(\omega k_\parallel)}{\sum_j w_j} \sum_j \frac{w_j}{v_{\perp,j}} \sum_{n=-\infty}^\infty \left(c_{m,j} Z(\tilde{\xi}_{n,j}) - \frac{1}{2} d_{m,j} Z'(\tilde{\xi}_{n,j}) \right) \\ &= \frac{q^2}{\varepsilon_0 \omega k_\parallel m V} \sum_j \frac{w_j}{v_{\perp,j}} \sum_{n=-\infty}^\infty \left(c_{m,j} Z(\tilde{\xi}_{n,j}) - \frac{1}{2} d_{m,j} Z'(\tilde{\xi}_{n,j}) \right), \end{aligned} \quad (27)$$

with k_\parallel the parallel wavenumber. This is just the contribution of one marker species, if more species exist one has to sum over those too. See the appendix for all of the coefficients. The plasma frequency ω_p is computed using the density, which is obtained by binning markers in space. So there is no need to compute ω_p^2 explicitly, instead the binning volume V can be used as is shown in the second line of Eq. (27). In general, $K_6 \neq K_4, K_7 \neq K_5$, so the dielectric tensor is written as:

$$\check{\mathbf{K}} = \begin{pmatrix} K_1 + K_0 \sin^2(\psi) & K_2 - K_0 \cos(\psi) \sin(\psi) & K_4 \cos(\psi) + K_5 \sin(\psi) \\ -K_2 - K_0 \cos(\psi) \sin(\psi) & K_1 + K_0 \cos^2(\psi) & K_4 \sin(\psi) - K_5 \cos(\psi) \\ K_6 \cos(\psi) - K_7 \sin(\psi) & K_6 \sin(\psi) + K_7 \cos(\psi) & K_3 \end{pmatrix}, \quad (28)$$

with ψ the wave phase. In order to get a proper representation of the underlying distribution function it must be sampled sufficiently. This can be achieved by running the PIC model until steady state is reached, after which marker data will be saved for each time step. If necessary, more data can be accumulated by simply running the model for more time steps after reaching steady state. If the time between saving the states is sufficient the associated marker data can be counted as independent samplings. If not, it will not yield worse statistics, but it just wastes computing time in the computation of Eq. (27). A comparison against a Maxwellian distribution is given in Section 4.

3. Comparison of the hot and warm dielectric tensor models

In this Section various different RF heating schemes are compared for JET plasmas, see table 2. To isolate the effect of the different dielectric tensors, only the wave code LEMan was ran. Because of axisymmetry the different toroidal modes n_{tor} decouple, and Eq. (9) can be solved independently for each one. In this Section only the single most important mode ($n_{tor} = 27$) is used. Of course this implies that the wave field is not localised, but spread out along the entire ϕ direction (2D model). The full SCENIC suite will be used in Section 5, in which more toroidal modes are included as well.

Table 2: Overview of the four JET cases studied in this paper. Species concentration in parentheses, $N(s)/N_e(s)$ for the regular (Bi-)Maxwellian, and analogously $N(s, B_C)/N_e(s)$ for the modified Bi-Maxwellian. Note these plasmas are quasi-neutral because $\sum_S q_S N_S = 0$, with S the species, including electrons. And analogously $\sum_S q_S \langle N_S \rangle = 0$ for the plasmas with a modified Bi-Maxwellian as minority distribution.

Case	A	B	C	D
Bulk ion species (N/N_e)	D(0.99)	D(0.98)	D(0.49), T(0.49)	D(0.32), T(0.64)
Minority ion species (N/N_e or $N(s, B_C)/N_e(s)$)	H(0.01)	^3He (0.01)	^3He (0.01)	^9Be (0.01)

All of these JET simulations used $\omega = B_0 q_{min}/m_{min}$ (so fundamental on axis heating), $B_0 = 2.7$ T, 201 poloidal modes and a grid resolution of $250 \times 400 \times 20$ (radial \times poloidal \times toroidal). Note that LEMan uses both poloidal and toroidal mode numbers, as well as a poloidal and toroidal grid, see Section 5.1. Typical plasma profiles were used, see figure C1, with $T_e = T_i$ and peak values of $T_e = 8.7$ keV, $N_e = 7.8 \cdot 10^{19} m^{-3}$. The simulations presented in this work always used a Maxwellian distribution for the background species. For the minority species the modified Bi-Maxwellian from Eq. (12) was used, unless specified otherwise. The regular and modified Bi-Maxwellians used an anisotropy $T_{\perp}/T_{\parallel} = 3$ and $T_{\parallel} = T_e$. In addition, the expansion of the dielectric tensor is to the same order in k_{\perp} for all species. So if one species used a warm model, so did the rest.

Note that the wave model is linear. This means that the coupled power does not enter the model as an input, and the final solution for the electric field can be scaled up/down arbitrarily. In this Section the presented electric field (and thereby the RF power density) have been scaled such that the total absorbed power is 4.5 MW. To obtain the result for a different coupled power P_c , the corresponding electric field will need to be multiplied by $\sqrt{P_c/4.5\text{MW}}$. However, the orbit tracer VENUS-LEVIS is not

Table 3: Absorbed power fractions (%) on each of the species rounded to two significant figures. The dielectric tensor model for the minority ions is indicated within parentheses. Warm here refers to the limiting case $k_{\perp} \rightarrow 0$. Hot includes FLR effects to all orders. “Bi-Max” refers to the regular Bi-Maxwellian from Eq. (10), and “mod Bi-Max” is the distribution from Eq. (12).

Case	Electrons	H	D	T	^3He	^9Be
A (Warm mod Bi-Max)	0.76	99	0.0	-	-	-
A (Hot Maxwellian)	29	30	41	-	-	-
A (Hot Bi-Max)	29	29	42	-	-	-
A (Hot mod Bi-Max)	29	29	42	-	-	-
B (Warm mod Bi-Max)	1.2	-	3.9	-	95	-
B (Hot Maxwellian)	47	-	2.0	-	51	-
B (Hot Bi-Max)	47	-	2.0	-	51	-
B (Hot mod Bi-Max)	47	-	2.0	-	51	-
C (Warm mod Bi-Max)	1.1	-	4.5	0.0	94	-
C (Hot Maxwellian)	31	-	2.9	15	51	-
C (Hot Bi-Max)	31	-	2.9	15	51	-
C (Hot mod Bi-Max)	31	-	3.0	15	51	-
D (Warm mod Bi-Max)	0.80	-	51	0.18	-	48
D (Hot Maxwellian)	9.5	-	47	0.16	-	43
D (Hot Bi-Max)	9.5	-	47	0.15	-	43
D (Hot mod Bi-Max)	9.1	-	47	0.16	-	43

linear w.r.t. the electric field, hence in Section 5.1 where the full SCENIC suite is used the coupled power does matter.

The most notable difference between the warm and hot model are the power fractions, which are summarised in table 3. The warm model does not have FLR corrections (zeroth order in k_{\perp}), which means that higher harmonic heating is not taken into account. This explains the lack of deuterium heating in case A and tritium heating in case C. In addition, the electron heating fraction is significantly underestimated in the warm model. The biggest FLR correction to heating at $n = 0$ is transit time magnetic pumping (TTMP), which originates from the parallel gradient of the magnetic field $\nabla_{\parallel}|\mathbf{B}_1|$, hence power absorption by this mechanism is proportional to $|\mathbf{k}_{\perp} \times \mathbf{E}_{\perp}|^2$. Even though $\frac{k_{\perp}^2 v_{T\perp}^2}{\Omega^2} \ll 1$ for electrons, TTMP can still be considerable because it uses the much larger transverse component of \mathbf{E}_1 , not the parallel one as in Landau damping. The power deposition is shown in more detail for case A in figure 4. The plotted poloidal slices are located at an arbitrary geometric toroidal angle, 0 in this case for convenience. The

antenna is centred at 293° , but the exact angle is unimportant in this simulation as just one toroidal mode is used. All species have a spike in power density on axis, which is coloured white because it is outside of the colour bar range. The cumulative power in figure 5 indicates absorbed total power within a flux surface with label $\rho = \sqrt{s}$, divided by total RF input power. Note that the modelling domain does not extend beyond the last closed flux surface (LCFS) because of the chosen (fixed boundary) equilibrium. So the RF antenna^{||} is modelled as a sub volume located at $\rho < 1$, hence all antenna power is coupled to the plasma in these simulations because no fast wave evanescent layer in the scrape off layer is considered. Therefore the cumulative power fractions recover the values from table 3 at the LCFS ($\rho = 1$).

Differences are also observed in the electric field. Due to the boundary conditions imposed in the model at $\rho = 1$, no RF power can leave through the LCFS. This means that the wave bounces around inside the plasma until it is absorbed. The warm model lacks some damping mechanisms, which causes the wave to propagate further, as is seen in figure 6. In addition, the wave field is slightly more focussed in the hot model w.r.t. the warm model. However, both models suffer from numerical artefacts near the magnetic axis. A tiny distortion results in a large k_\perp using the gradient method (described in Appendix B of [13]). The warm model uses a dielectric tensor to zeroth order in k_\perp , so it is unaffected by the value of k_\perp . And so the power deposition is not altered. On the other hand, for the hot model this artefact does propagate into the dielectric tensor, and therefore into the power deposition as well. However, this distortion does not significantly impact the total power deposition, due to the volume effect. This can be seen in the cumulative power, figure 5.

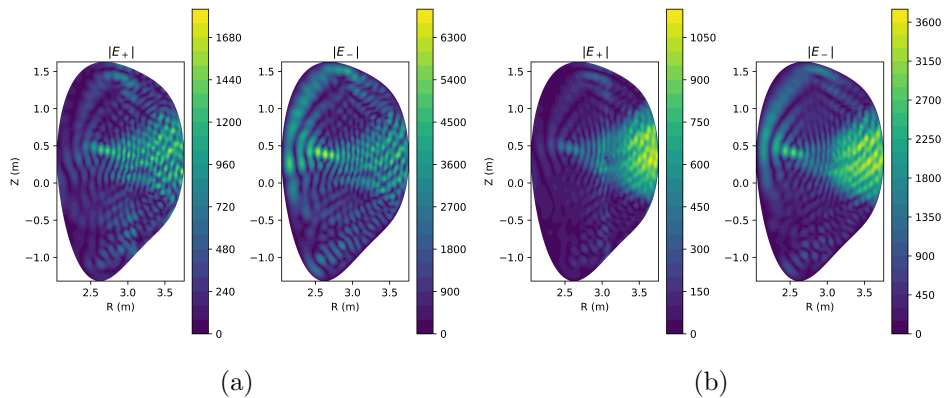


Figure 6: Left and right handed polarised wave components, in V/m, plotted at a geometric toroidal angle of 0 for case A. The warm model on the left, the hot model on the right.

^{||} See Section 3.1 of Ref. [41] and Section 3.5 of Ref. [14] for a detailed description of the LEMan antenna models.

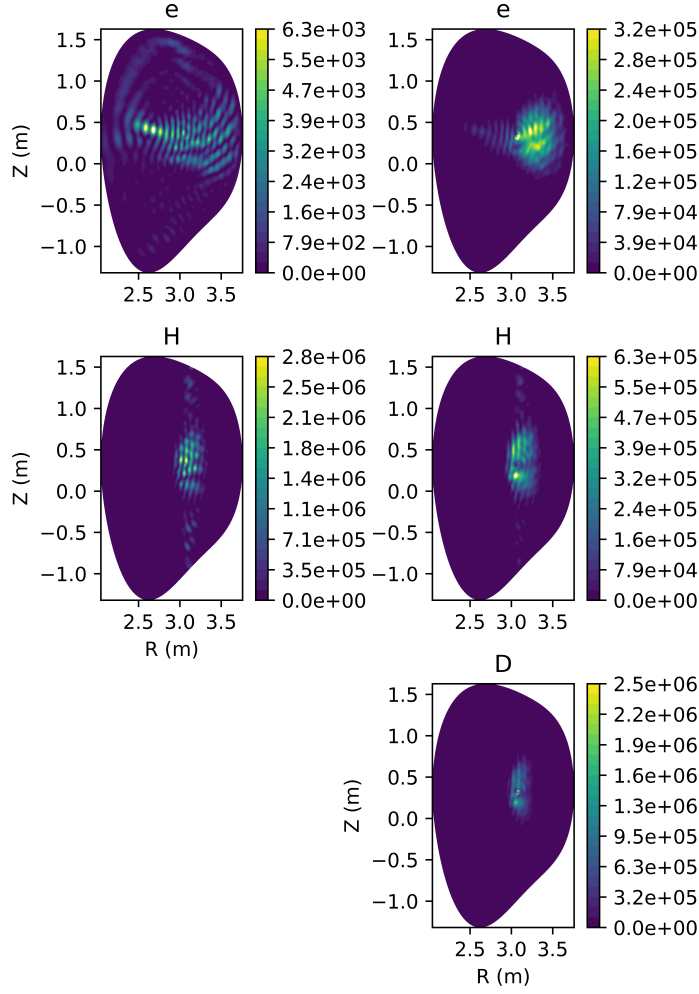


Figure 4: Absorbed power densities on each species in the contour plots for case A, in MWm^{-3} . The left column is for the warm model, the right for the hot model. Power on deuterium is not shown for the warm model as it is zero (no 2nd harmonic heating) up to machine precision errors.

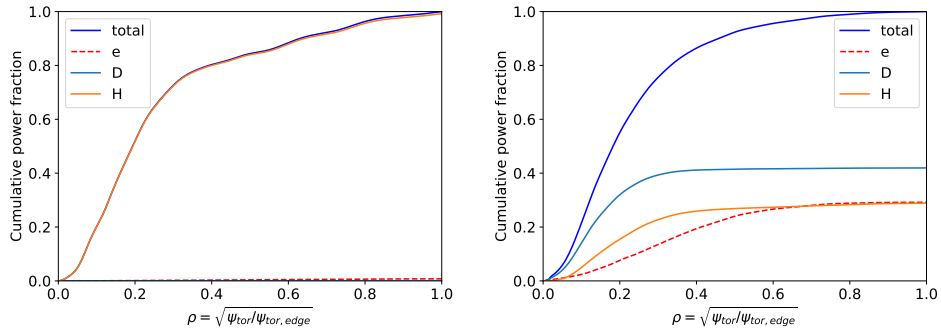


Figure 5: Cumulative power fractions for each species in case A, versus radial position. The warm model on the left, the hot model on the right.

In cases A,B and C the electron power is rather high. This is because the minority species used here is thermal (not fast), and it is only 1%. A higher ion heating fraction may be obtained at larger concentrations, simply because there are more minority ions to absorb power. However, at too large minority concentration it is no longer a “minority”, and polarisation at the fundamental becomes unfavourable. In addition, at large concentrations the electron power is increased through Landau damping of the mode converted wave. The latter effect is not included by LEMan. In case B the electron power is highest, this is because it does not benefit from the second harmonic heating of case A, C. The bulk deuterium resonates at the fundamental frequency, meaning the polarisation is unfavourable.

Case D is selected for its enhanced power deposition on ions. The ITER like wall (ILW) of JET is made partly of beryllium, so the plasma will contain beryllium as an impurity species. Instead of adding a minority species for RF heating, such native impurities can be used for fundamental cyclotron heating. In addition a 3-ion scheme can be constructed by tuning the concentrations of other ion species. This will optimise the wave polarisation by approximately lining up the L cut-off with the ^9Be cyclotron resonance [42], see the narrow layer of enhanced $|E_+|$ in figure 7a. All ion resonances in the plasma are at the fundamental for this case: From LFS to HFS, the deuterium resonance is encountered first, followed by the Be and then the T resonance. The power on T is insignificant because the polarisation is unfavourable, and most power has already been absorbed by the other species before the wave reaches the HFS resonance, see figure 8. Deuterium effectively absorbs power because its resonance is close to that of beryllium, and therefore it also profits from the enhanced polarisation. The simulation is converged, as is seen in the poloidal spectrum, figure 7b. The Fourier mode amplitudes of the electric potential depend also on the selected flux surface, therefore the average and maximum over the radial s grid are shown.

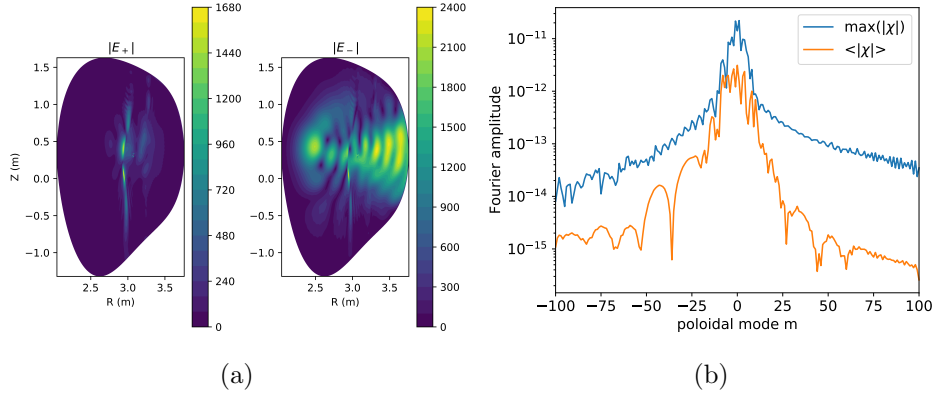


Figure 7: Left and right handed polarised wave components for case D, in V/m. On the right the Fourier mode amplitudes (arbitrary units) of the electric potential χ are shown for the same simulation.

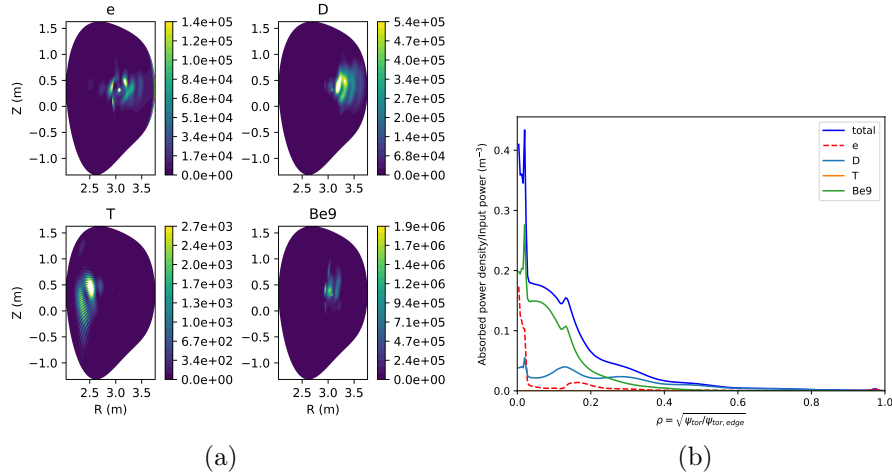


Figure 8: Absorbed RF power density in MWm^{-3} , for all of the plasma species, case D. In the right plot the volume averaged power density is shown versus radial coordinate ρ .

Even though “on-axis” heating of Be was used, the average power is not maximal exactly at $s = 0$ in case D. The plasma does work as a lens to some extent for the ICRF waves, focussing it towards the axis. In addition, the antenna straps are designed to approximately match the shape of the LCFS. However, it still has a non-zero wavelength, the resonance layer has a vertical extension, and the interference of the wave with its reflected signal (from the wall or a cut-off) can displace the maximum.

4. Comparing PIC dielectric tensor against Maxwellian

The JET cases of table 2 used an analytic expression for the distribution function. However, PIC data can function as a substitute for the minority distribution function,

as was shown in Section 2.3. In order to verify the implementation of Eq. (27) in LEMAN, it has been applied to JET case A for a Maxwellian distribution function (for all species). See figure 9 for the power deposition, compared against the corresponding case from Section 3. Note the negative power in the left most case, as well as in the second case (close to the axis). A sharp eye will catch that in all cases, including the reference case, there are regions of negative power outside of the core. But this is just machine precision noise which can be ignored. From left to right the power fractions (%) are e(34), D(47), H(19); e(30), D(43), H(28); e(29), D(41), H(30) and e(29), D(41), H(30). Agreement of the last two cases demonstrates convergence.

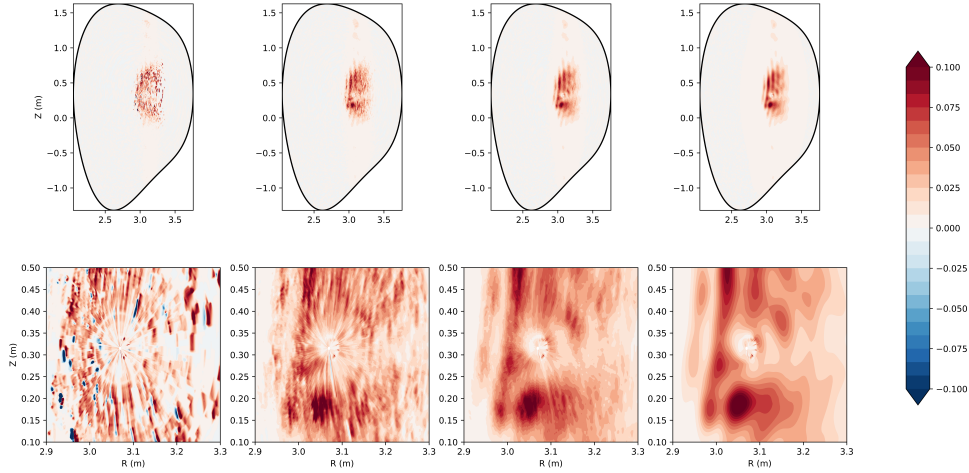


Figure 9: D-(H) minority heating, H power density shown. From left to right the columns correspond to cases with 10^5 , 10^6 , 10^7 markers using the PIC dielectric tensor, and the fourth column shows the Maxwellian reference case (no markers). The power density has been cropped at ± 0.1 in arbitrary units. The bottom row of panels shows a zoom of the core region. No data is available exactly on axis, hence the white dot in the centre.

VENUS-LEVIS has been used to read in the equilibrium data and initialise a given number of markers. The binning widths $\Delta s = 0.01$, $\Delta\theta = 0.16$ rad, $\Delta\varphi = \infty$ were used. I.e. toroidal symmetry has been assumed, so no binning in toroidal direction is necessary which means excellent statistics can be obtained at a reasonable computational cost. The smoothing parameter σ_j from Eq. (21) is chosen to be 40 km/s for all markers. With a sufficient amount of markers the reference case is reproduced, see figure 9. In this particular case 10^5 is woefully insufficient, but 10^6 agrees well with the reference case. Of course for more exotic distributions a smaller binning width may be required, as well as a smaller smoothing parameter σ_j .

In summary, the disadvantages of this PIC approach compared to assuming an analytic distribution function are:

- It takes more CPU hours to get the same result. The PIC runs took about 13.5, 15.1, 126.7 node hours for $10^5, 10^6, 10^7$ markers respectively. The Maxwellian reference case only took about 0.7 node hours. In the limit of large marker counts the wall time scales linearly with this count, since computing each marker's contribution is independent, thus it is also easy to parallelise. But for relatively small marker count other parts of the code dominate CPU time. Hence, the small difference in wall time between the 10^5 and 10^6 marker run.
- Noise. As seen in figure 9, the grainy nature of the distribution is visible. But worse, it can also lead to negative power deposition if the marker count is too low. The lack of markers is especially prevalent in the region close to the LCFS. However, this is not very important because the PIC approach will only be applied to the minority species. Because of its low concentration the minority species only weakly affects the total dielectric tensor, and therefore the electric field. Secondly, where the minority density is low, the power absorption is expected to be small as well. Hence, noise is more detrimental to the core.
- There are more model inputs to include, namely, the smoothing and binning parameters.

However, an advantage of the PIC approach is that no input profiles of the minority species are required, just the marker data. So temperature, density (-factor), anisotropy, etc need not be constant on a flux surface. This means that more physical effects can be included, given a sufficient marker count.

5. SCENIC iteration in JET

In the previous sections the equilibrium distribution function was assumed to be fixed, as well as the magnetic equilibrium. However, fast ion populations are known to be generated by RF and they can affect the magnetic equilibrium, which will be investigated in this section with SCENIC for JET case A.

5.1. SCENIC code

In this work the code package SCENIC has been used, consisting of three separate codes: ANIMEC, LEMan and VENUS-LEVIS. SCENIC iterates multiple times until a converged solution is found. The first code is an anisotropic flavour of VMFC [43]. The magnetic equilibrium is computed assuming nested magnetic flux surfaces. However, temperature anisotropy $T_{\perp} \neq T_{\parallel}$ is allowed. This is often the case in ICRF heating scenarios, where $T_{\perp} > T_{\parallel}$. LEMan is a hybrid code, using finite elements (cubic polynomials) in the radial direction, and a spectral method in poloidal and toroidal direction. It computes the electric (and magnetic) field of the RF wave in 2D or 3D,

as well as collisionless power deposition. In order to compute the volume integrals that appear in the finite element method, certain quantities need to be sampled on a grid. These include the wave vector, dielectric tensor, antenna current density, and more. Gaussian quadrature with five points is used for integration in radial direction. This means that every radial interval is divided into five flux surfaces. Each of these surfaces is discretised into a given number of points, e.g. 400×20 (poloidal \times toroidal) for JET. The dielectric tensor is computed on each of these points, using only one, effective, wave vector per point. The finer the grid, the more accurate the integrals will be, but the number of grid points need not be equal to mode numbers, as is the case in some other (pseudo-) spectral full wave codes. VENUS-LEVIS is an orbit tracing code used to compute the updated equilibrium distribution function f_0 . It is a stochastic model, using Monte Carlo kick operators for collisions and interaction with the wave field. It can run in full 6D mode, or 4D mode (guiding centre position and parallel velocity). The latter is used for ICRF modelling. Furthermore, it can compute NBI deposition, so where the neutrals are ionised, and the slowing down population can be modelled. In addition, collisional power is computed. SCENIC exploits the separation of time scales: The time required for the RF wave to propagate through the plasma is much smaller than the time on which the equilibrium distribution function f_0 changes. This means that the wave field can be computed with a frozen in equilibrium distribution function, so a linear Helmholtz type equation is solved. Once this linear RF electromagnetic field is computed, its Fourier amplitudes can be assumed frozen in, and the non-linear evolution of f_0 over the scale of milliseconds is done. The combined approach is referred to as “quasilinear”. This second step is done by VENUS-LEVIS. The bulk of the computation time for SCENIC is spent in VENUS-LEVIS. This code is written in modern Fortran, using features from the 2003 standard. It furthermore employs MPI for parallelism.

5.2. SCENIC simulation of D-(H) minority heating in JET

In order to accurately model the toroidal localisation of the RF antenna, more than one toroidal mode needs to be used. For this purpose the most important modes are sampled from the antenna current spectrum. In case of dipole phasing, which is used here, the usual modes are $n_{tor} = \pm 13, \pm 27$. For VENUS-LEVIS the relative amplitudes are required, but these too are known from the antenna spectrum, see table 3.2 in Ref.[14].

In order to reach steady state, VENUS-LEVIS simulated 100 ms of physical time, the last 50 ms are used for analysis. A total number of 2002944 markers were used, with data recorded every 1 ms. This takes about 5 hours per VENUS-LEVIS run, on 128 Intel Xeon 8160 CPUs (3072 cores total). The coupled RF power is assumed to be 4.5 MW, which has been scaled down to 40%, i.e. about 1.81 MW, which is the power fraction of hydrogen. The electric field computed by LEMan is rescaled such that VENUS-LEVIS retrieves this power deposition. Note, that 40% is larger than what is found in table 3. This correction is mainly due to the modification of the distribution

function after running VENUS-LEVIS.

The effect of the fast ions on the magnetic equilibrium is taken into account. The effect is limited because this ANIMEC run used a fixed boundary, i.e. the LCFS is prescribed as a boundary condition. However, the flux surfaces inside can still shift around. The minority species modifies the pressure tensor, as well as the toroidal current profile. However, the total toroidal plasma current was fixed to 2.2 MA. One way to gauge the convergence of SCENIC is the distribution function, see figure 10.

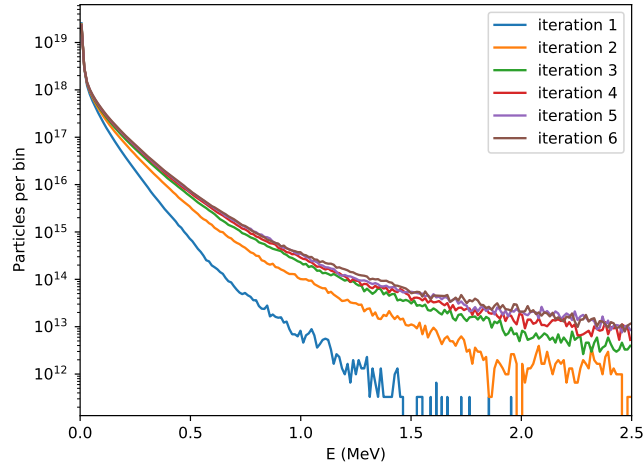


Figure 10: Energy histogram of H minority ions, after 6 consecutive SCENIC iterations, 200 bins used.

The anisotropy of the fast particles is considerable, see figure 11. Note, the 2D histograms in figure 11 bin all of the fast H ions in the plasma. The RF wave drives ions into the MeV range, but most of these high energy particles are deeply trapped. Moreover, a parallel velocity asymmetry is visible (more particles with $v_{\parallel} > 0$). Note that even though a symmetric antenna spectrum has been used, this does not in general imply a symmetric distribution of v_{\parallel} . One reason is that resonance with different parts of the mode spectrum happens at different places in the plasma due to the Doppler shift ($\omega = k_{\parallel}v_{\parallel} + n\Omega$). Collisional power is peaked on axis, shown in figure 12. In addition to direct absorption of the RF power on electrons, they can also gain power through collisions with the fast ions driven by the wave. Collisional heating of ions and electrons is approximately equal in this scenario. However, the latter would dominate at larger antenna power due to the further enhancement of the fast ion tail. Additionally, the fast ion pressure is not a flux function, see figure 13. As explained before, trapped ions that intersect the resonant surface approximately line up their bounce points with the surface, resulting in an accumulation on the LFS. VENUS-LEVIS models the trajectories of these trapped ions, including the finite orbit width. LEMan is able to inherit these qualities to some extent by using the marker distribution (or its moments) in its computation of the dielectric tensor.

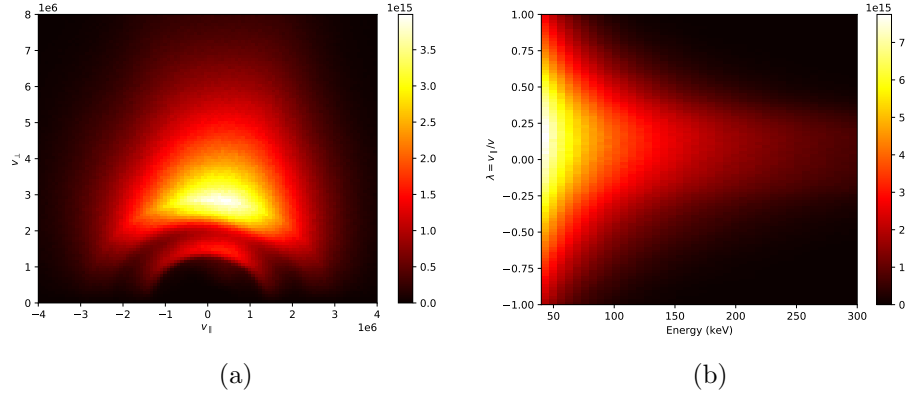


Figure 11: 2D histograms of the fast H minority population, markers with $E/T_e < 5$ are omitted from the left plot. The colourbar shows the number of particles per bin. 40 Bins in energy space, 100 bins for the velocity components and the pitch angle.

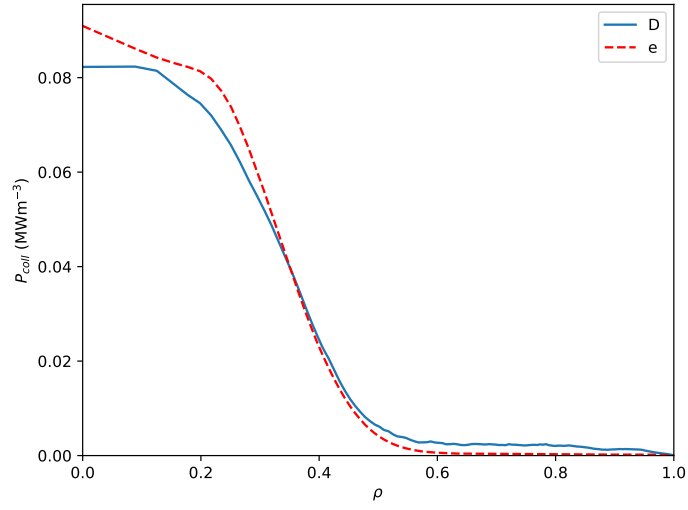


Figure 12: Collisional power density of hydrogen on background species versus radial position, averaged over angular coordinates.

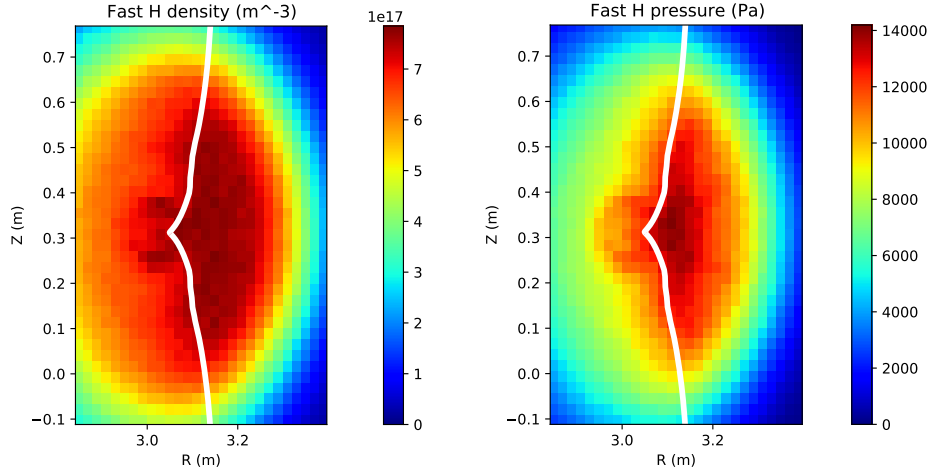


Figure 13: Fast ion density (left) and fast ion pressure (right) in the core (averaged over toroidal angle), protons with kinetic energy less than five times the local electron temperature are not plotted. The white line indicates the cold plasma resonance $B = B_C$.

6. Minority heating in W7-X

In the previous sections the hot plasma model was studied using the modified Bi-Maxwellian in 2D magnetic configurations, in this section it will be applied to 3D plasmas. In order to isolate the wave part of the ICRH problem only LEMan will be used, not the whole SCENIC suite. Contrary to the tokamak simulations, a different antenna model was used for W7-X. Instead of decomposing it in toroidal modes, a fully localised antenna current is used, see Section 3.5 of Ref. [14]. ^4He -(H) minority heating is one of the planned RF schemes for the initial stage of the second operational phase in W7-X. In addition, it is reasonable to assume some carbon is released from the wall, which will also absorb power through second harmonic heating. To be able to model the power fractions accurately in this scenario the hot model is required. A standard mirror equilibrium with on axis heating (2.5 T) was used, with 1% H, 0.5% $^{12}\text{C}^{6+}$ and the rest ^4He . Plasma profiles are shown in Appendix C. For the H minority species the modified Bi-Maxwellian was used with temperature anisotropy of 3. LEMan used 30 poloidal \times 300 toroidal modes, spread over 5 separate simulations. The grid resolution was 200 \times 300 \times 250 (radial \times poloidal \times toroidal). The electric field of the wave and power deposition are depicted in figure 14, figure 15.

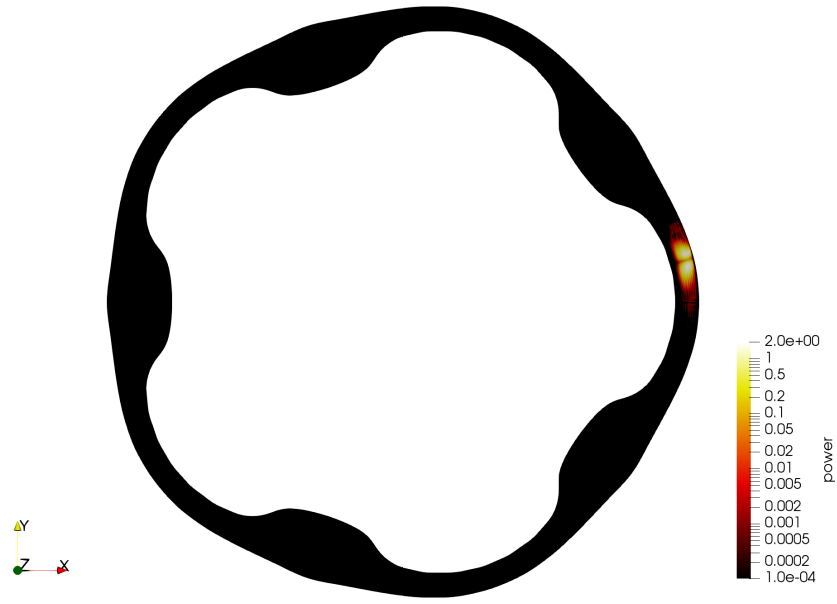
It is important to use a sufficient amount of poloidal and toroidal Fourier modes to achieve proper convergence, see figure 16 for an example spectrum in W7-X. In W7-X just one RF antenna will be deployed (and is modelled here), this means that the wave field, and the associate power deposition are highly localised around the antenna, see figure 14, figure 15. If too few modes are used the electric field of the RF wave will

propagate further into the other 4 periods of the machine and deposit power there as well. In addition, in the ICRF electrons only resonate with $v_{\parallel} = \omega/k_{\parallel}$, matching the parallel phase velocity of the wave. In LEMan an effective parallel wave number is derived from the electric potential $\hat{\chi}$ using the parallel gradient: $k_{\parallel} = |\nabla_{\parallel}\hat{\chi}|/|\hat{\chi}|$. Having enough toroidal modes is absolutely vital for getting the power deposition to the electrons right. Otherwise this effective parallel wave number is too small, and thus the phase velocity will be too high. Because of the exponential drop off with energy of the Maxwellian distribution for the electrons, a negligible amount is fast enough to still resonate. This was not an issue for the JET simulations since only the most important toroidal modes are used instead of a dense spectrum.

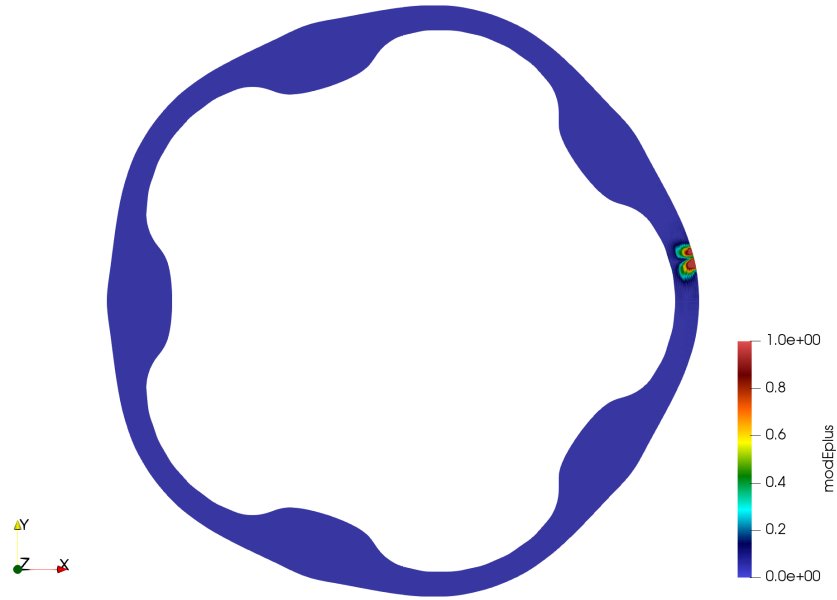
However, in 3D in general all Fourier modes of the RF wave couple together, i.e. all mode amplitudes have to be solved for simultaneously. Matrix construction in the spectral code scales as $O(N^2)$, with N the number of modes. For large problem sizes the Gaussian elimination step dominates solution time but this scales even worse, $O(N^3)$. This makes simulations at large N prohibitively expensive. Fortunately, an optimisation is possible for plasmas that have toroidal periodicity, and with an antenna in one field period only [44]. This means that not all modes couple together: For W7-X the toroidal modes can be distributed over five independent (interlaced) families. E.g. the first family has toroidal modes $n_{tor} = -150, -145, -140, \dots, 145$, the second has $n_{tor} = -149, -144, -139, \dots, 146$ and so on. As all families can run concurrently, the wall time is just the required run time of one family. But a “monolithic” run, so all modes in one simulation, would take between 25 and 125 times longer.

Moreover, a scan in H concentration has been performed, see figure 17. The power on C is about 100 times lower than that on He. This is expected because the concentration is only 0.5% and in this scheme it only absorbs power through second harmonic heating[¶]. Increasing the carbon concentration at the cost of helium (3 He for 1 C) will decrease the ion power fraction. The plasma frequency is not affected but carbon has a smaller thermal velocity than helium (same temperature assumed), resulting in a narrower resonance layer. In other words, the effect of the Doppler shift on the power absorption is less strong for carbon, $|Z(\zeta_{n,C})/Z(\zeta_{n,He})| = |Z(\sqrt{3}\zeta_{n,He})/Z(\zeta_{n,He})| \leq 1$. As was already explained in Section 3, the ion power fraction can be improved by using a higher ion temperature, e.g. through the addition of a beam species. Alternatively, the ^4He can be replaced with D to increase the thermal velocity and therefore broaden the resonance layer. Or a different scheme can be used that is more optimised such as the JET case D. Furthermore, in these W7-X simulations the electron density is rather high, which results in considerable damping on electrons close to the antenna. This is before the wave even encounters the minority resonance. So using off-axis heating, on

[¶] In this scheme the effect of carbon impurities is minimal, but that is certainly not always the case. E.g. in the inverted scheme H-(^4He) or H-(D) with carbon it could play a much more significant role. In those schemes a carbon concentration of a few percent can lead to significant mode conversion [45, 3].



(a)



(b)

Figure 14: Absorbed power density on hydrogen minorities in W7-X on the top. Most absorption happens right in front of the antenna, which is placed roughly at a geometric toroidal angle of 8 degrees. On the bottom a plot of the left handed polarised wave component $|E_+|$. Arbitrary units.

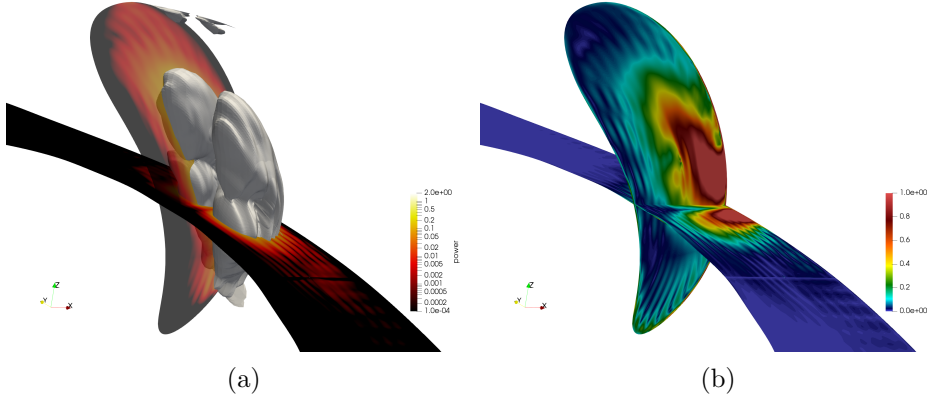


Figure 15: Zoom of the antenna region. The power deposition on hydrogen is shown on the left, $|E_+|$ on the right. The white surface in the figure (a) highlights a sub volume where the power density exceeds 0.1 (A.U.). The poloidal slice is placed at a geometric toroidal angle of 8 degrees, which is approximately bisects the antenna.

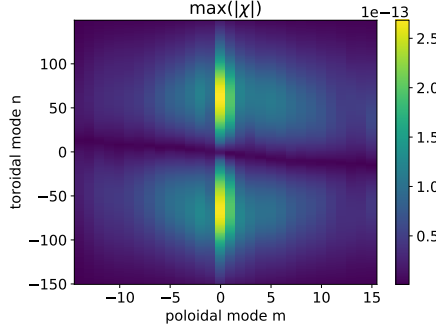


Figure 16: Fourier mode spectrum. Here χ represents the m, n Fourier amplitude of the electric potential. The maximum of $|\chi|$ over the radial domain is plotted.

the LFS, or using more peaked density profiles may result in an improved ion heating fraction.

7. Conclusion

In many common RF heating scenarios FLR effects play a significant role, as was observed for the JET cases A, B and C. In order to accurately simulate these cases the dielectric tensor model of LEMan has been upgraded. It now features a dielectric tensor for the modified Bi-Maxwellian, accurate to all orders in FLR. The main differences compared to the warm model are the species power fractions. Secondly, the RF wave field is more focussed in the hot plasma model. For case D the warm model suffices, as it involved no higher harmonic heating and electron power was limited.

Moreover, another new dielectric tensor has been presented that can take in PIC data as a substitute for the minority distribution, avoiding the need to fit the PIC

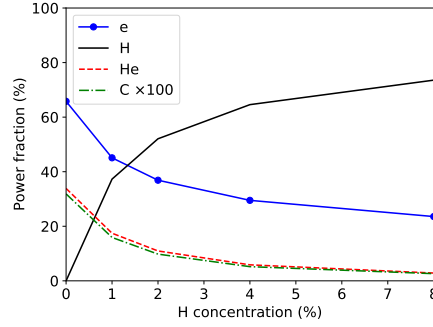


Figure 17: The RF heating power partitions for all plasma species given a H concentration of 0, 1, 2, 4 and 8%. The $^{12}\text{C}^{6+}$ concentration was fixed to 0.5% and the rest is ^4He . For visibility, the power fraction of carbon has been multiplied by 100 in this plot.

data. Contrary to the derivation for the modified Bi-Maxwellian, the velocity space integration was performed analytically. The new dielectric tensor was compared against a Maxwellian reference case for JET, and was shown to converge correctly. This is promising for modelling more exotic distribution functions in the future, such as the NBI slowing down distribution.

The distribution of fast ions was presented for a D-(H) minority heating case in JET. This was computed self consistently using SCENIC. It was found that the collisional power is shared approximately equally between background ions and electrons in this scenario. In the future more JET cases are planned to be investigated with SCENIC, including advanced heating schemes such as the 3-ion scheme.

Lastly, ^4He -(H) minority heating was simulated in W7-X, including C impurities. The RF power is deposited very close to the antenna, with negligible power and electric field making it into the other four periods of the device. Of course the minority ions that are heated by the RF wave do not remain near the antenna and will deposit power elsewhere. Their confinement properties in the 3D plasma of W7-X are of interest as well, which will be investigated further with SCENIC in the future.

Acknowledgments

This work has been carried out within the framework of the EUROfusion consortium and has received funding from the Euratom research and training programme 2014-2018 and 2019-2020 under grant agreement No 633053. The views and opinions expressed herein do not necessarily reflect those of the European Commission. The project was also supported in part by the Swiss National Science Foundation. The Piz Daint (CSCS, Switzerland) and the MARCONI-Fusion (CINECA/ENEA, Italy) supercomputer facilities were used for the simulations presented in this research. Numerical calculations were supported by a grant from CSCS under project ID s1087,

and project FUA35_VENUSLEV for CINECA.

Appendix A. K elements modified Bi-Maxwellian

Appendix A.1. High field side

On the HFS ($B \geq B_C$), $E - \mu B_C \geq 0$ always, so the absolute value signs can be removed. The distribution function on this side can be written as:

$$\begin{aligned} f_0(v_\perp, v_\parallel) &= \frac{1}{\mathcal{C}} \frac{NF(v_\parallel)}{\pi v_{T_\perp}^2} e^{-(v_\perp^2/v_{T_\perp}^2)C_+} \\ C_\pm &= \frac{B_C}{B} \pm \frac{T_\perp}{T_\parallel} \left(1 - \frac{B_C}{B}\right) \\ F(v_\parallel) &= \frac{1}{\sqrt{\pi} v_{T_\parallel}} e^{-v_\parallel^2/v_{T_\parallel}^2} \end{aligned} \quad (\text{A.1})$$

Note, for $B \geq B_C$, $C_+ \geq 0$, and for $B < B_C$, $C_- \geq 0$ always. Eq. (A.1) is similar to the distribution function used in Section 4.3.4 of Ref. [32]. Simply replacing $v_{T_\perp} \rightarrow v_{T_\perp}/\sqrt{C_+}$, $T_\perp \rightarrow T_\perp/C_+$, $\lambda \rightarrow \lambda/C_+ = \frac{k_\perp^2 v_{T_\perp}^2}{2\Omega^2 C_+}$, and tacking on $(\mathcal{C}C_+)^{-1}$ yields the result. With FLR parameter defined as $\lambda = \frac{1}{2}\rho_{T_\perp}^2 k_\perp^2 = \frac{v_{T_\perp}^2 k_\perp^2}{2\Omega^2}$. Using $N/\mathcal{C} = \mathcal{N}\sqrt{\frac{T_\parallel}{T_\perp}}$ the \mathcal{C} can be eliminated.

So the contribution of one species to the dielectric tensor in hot plasma, for the (non-relativistic) modified Bi-Maxwellian with no parallel drift velocity, for $B > B_C$ is:

$$\check{\mathbf{K}} = \begin{pmatrix} K_1 + K_0 \sin^2(\psi) & K_2 - K_0 \cos(\psi) \sin(\psi) & K_4 \cos(\psi) + K_5 \sin(\psi) \\ -K_2 - K_0 \cos(\psi) \sin(\psi) & K_1 + K_0 \cos^2(\psi) & K_4 \sin(\psi) - K_5 \cos(\psi) \\ K_4 \cos(\psi) - K_5 \sin(\psi) & K_4 \sin(\psi) + K_5 \cos(\psi) & K_3 \end{pmatrix} \quad (\text{A.2})$$

With ψ the phase of the wave vector in the plane perpendicular to \mathbf{B} :

$$k_n = k_\perp \cos \psi, \quad k_b = k_\perp \sin \psi, \quad (\text{A.3})$$

where k_n, k_b are the normal and binormal components respectively, see Appendix B of

Ref. [13]. And the elements are:

$$\begin{aligned}
K_0 &= 2\sqrt{\frac{T_{\parallel}}{T_{\perp}} \frac{\tilde{\omega}_p^2 e^{-\lambda/C_+}}{\omega k_{\parallel} v_{T_{\parallel}} C_+}} \sum_{n=-\infty}^{\infty} \frac{\lambda}{C_+} (I_n - I'_n) \left[Z(\zeta_n) + \frac{k_{\parallel} v_{T_{\parallel}}}{\omega} \left(1 - \frac{T_{\perp}}{T_{\parallel} C_+} \right) \frac{Z'(\zeta_n)}{2} \right] \\
K_1 &= \sqrt{\frac{T_{\parallel}}{T_{\perp}} \frac{\tilde{\omega}_p^2 e^{-\lambda/C_+}}{\omega k_{\parallel} v_{T_{\parallel}} C_+}} \sum_{n=-\infty}^{\infty} \frac{n^2 I_n C_+}{\lambda} \left[Z(\zeta_n) + \frac{k_{\parallel} v_{T_{\parallel}}}{\omega} \left(1 - \frac{T_{\perp}}{T_{\parallel} C_+} \right) \frac{Z'(\zeta_n)}{2} \right] \\
K_2 &= i\sqrt{\frac{T_{\parallel}}{T_{\perp}} \frac{\epsilon \tilde{\omega}_p^2 e^{-\lambda/C_+}}{\omega k_{\parallel} v_{T_{\parallel}} C_+}} \sum_{n=-\infty}^{\infty} n (I_n - I'_n) \left[Z(\zeta_n) + \frac{k_{\parallel} v_{T_{\parallel}}}{\omega} \left(1 - \frac{T_{\perp}}{T_{\parallel} C_+} \right) \frac{Z'(\zeta_n)}{2} \right] \\
K_3 &= -\sqrt{\frac{T_{\parallel}}{T_{\perp}} \frac{\tilde{\omega}_p^2 e^{-\lambda/C_+}}{\omega k_{\parallel} v_{T_{\parallel}} C_+}} \sum_{n=-\infty}^{\infty} I_n \zeta_n \left[1 + \frac{n\Omega}{\omega} \left(1 - \frac{T_{\parallel} C_+}{T_{\perp}} \right) \right] Z'(\zeta_n) \\
K_4 &= \sqrt{\frac{T_{\parallel}}{T_{\perp}} \frac{k_{\perp} \tilde{\omega}_p^2 e^{-\lambda/C_+}}{\omega k_{\parallel} \Omega C_+}} \sum_{n=-\infty}^{\infty} \frac{n I_n C_+}{\lambda} \left[\frac{T_{\perp}}{T_{\parallel} C_+} - \frac{n\Omega}{\omega} \left(1 - \frac{T_{\perp}}{T_{\parallel} C_+} \right) \right] \frac{Z'(\zeta_n)}{2} \\
K_5 &= i\sqrt{\frac{T_{\parallel}}{T_{\perp}} \frac{\epsilon k_{\perp} \tilde{\omega}_p^2 e^{-\lambda/C_+}}{\omega k_{\parallel} \Omega C_+}} \sum_{n=-\infty}^{\infty} (I_n - I'_n) \left[\frac{T_{\perp}}{T_{\parallel} C_+} - \frac{n\Omega}{\omega} \left(1 - \frac{T_{\perp}}{T_{\parallel} C_+} \right) \right] \frac{Z'(\zeta_n)}{2}
\end{aligned} \tag{A.4}$$

And the plasma dispersion function [46]⁺ is here defined as:

$$Z(\zeta) = \frac{1}{\sqrt{\pi}} \int_{-\infty}^{\infty} \frac{e^{-x^2}}{x - \zeta} dx, \quad \text{Im}(\zeta) > 0 \tag{A.5}$$

The derivatives of which can be rewritten using the identity:

$$Z'(\zeta) = -2(1 + \zeta Z(\zeta)) \tag{A.6}$$

The modified plasma frequency is $\tilde{\omega}_p^2 = \frac{q^2 \mathcal{N}}{\epsilon_0 m}$, where density has been replaced by the density factor, $\epsilon = q/|q|$ indicates the charge sign, and $\zeta_n = \frac{\omega + n\Omega}{k_{\parallel} v_{T_{\parallel}}}$. Note, other books [31, 30] may use a different definition of ζ_n , with $-n$ in the numerator. This is also valid, as long as one is consistent. Symmetry can be used to rewrite it, $I_n(z) = I_{-n}(z)$. But care must be taken with terms as K_2 which contain a multiplication by n , thus tacking on another minus. Many other, equivalent forms of these expressions exist, e.g. the derivatives $I'_n(z)$ can be eliminated with the identity $I'_n(z) = \frac{n}{z} I_n(z) + I_{n+1}(z)$ or $I'_n(z) = I_{n-1}(z) - \frac{n}{z} I_n(z)$. Thus, also $I'_n(z) = I'_{-n}(z)$. Also note, the T_{\parallel}, T_{\perp} are **swapped** in K_3 . The modified Bessel functions in Eq. (A.4) have as argument λ/C_+ . Note, typically \mathcal{C} and C_+ are roughly equal to 1, and thus it is not a big deformation from the regular Bi-Maxwellian. Note, Eq. (A.4) is just the contribution of the fast species, no background species are included. To get the total dielectric tensor, sum over those too, and the identity matrix for the vacuum.

⁺ This is the Hilbert transform of a Gaussian. Beware, in other literature different definitions of the plasma dispersion function may be in use!

The modified Bessel functions are required, but these are not exponentially scaled by the special functions library. So these limiting expressions for large $|z|$ (with $Re(z) > 700$) are used to avoid floating point overflow:

$$I_n(z) \approx \frac{e^z}{\sqrt{2\pi z}} \left(1 - \frac{4n^2 - 1}{8z} + \dots \right) \approx \frac{e^z}{\sqrt{2\pi z}} \quad (\text{A.7})$$

Using a recurrence relation:

$$I'_n(z) \approx \frac{e^z}{\sqrt{2\pi z}} \left(1 - \frac{4n^2 + 3}{8z} + \dots \right) \approx \frac{e^z}{\sqrt{2\pi z}} \quad (\text{A.8})$$

The e^{-z} cancels with the e^z . For $Re(z) < 0$ (evanescent region), the zeroth order warm ($k_\perp \rightarrow 0$) expressions are used.

Appendix A.2. Low field side

On the LFS the following even functions are used in Eq. (16):

$$\begin{aligned} M_1(x) &= \int_0^\infty y e^{-|x^2 + by^2| - y^2} J_n^2(ay) dy \\ M_2(x) &= \int_0^\infty y^2 e^{-|x^2 + by^2| - y^2} J_n(ay) J'_n(ay) dy \\ M_3(x) &= \int_0^\infty y e^{-|x^2 + by^2| - y^2} [a^2 y^2 J_n'^2(ay) - n^2 J_n^2(ay)] dy \\ N_1(x) &= \int_0^\infty \text{sign}(x^2 + by^2) y e^{-|x^2 + by^2| - y^2} J_n^2(ay) dy \\ N_2(x) &= \int_0^\infty \text{sign}(x^2 + by^2) y^2 e^{-|x^2 + by^2| - y^2} J_n(ay) J'_n(ay) dy \\ N_3(x) &= \int_0^\infty \text{sign}(x^2 + by^2) y e^{-|x^2 + by^2| - y^2} [a^2 y^2 J_n'^2(ay) - n^2 J_n^2(ay)] dy \end{aligned} \quad (\text{A.9})$$

With $x = v_\parallel / v_{T\parallel}$, $y = \frac{v_\perp}{v_{T\perp}} \sqrt{\frac{B_C}{B}}$, $a = \frac{\epsilon k_\perp v_{T\perp}}{\Omega} \sqrt{\frac{B}{B_C}}$, $a^2 = 2\lambda \frac{B}{B_C}$, $b = \frac{T_\perp}{T_\parallel} \left(\frac{B}{B_C} - 1 \right)$, $\xi_n = \zeta_{-\epsilon n} = \frac{\omega - n\epsilon\Omega}{k_z v_{T\parallel}}$ and

$$\text{sign}(x) = \begin{cases} -1, & x < 0 \\ 0, & x = 0 \\ 1, & x > 0 \end{cases}$$

And

	K_0	K_1	K_2	K_3	K_4	K_5
Υ_l	$\frac{4\tilde{\omega}_p^2 \Omega^2 B}{\sqrt{\pi} \omega k_{\parallel} k_{\perp}^2 v_{T\perp}^3 B_C}$	$\frac{4\tilde{\omega}_p^2 \Omega^2 B}{\sqrt{\pi} \omega k_{\parallel} k_{\perp}^2 v_{T\perp}^3 B_C}$	$\frac{4i\tilde{\omega}_p^2 \Omega \epsilon B^{3/2}}{\sqrt{\pi} \omega k_{\parallel} k_{\perp} v_{T\perp}^2 B_C^{3/2}}$	$\frac{4\tilde{\omega}_p^2 v_{T\parallel}^2 B}{\sqrt{\pi} \omega k_{\parallel} v_{T\perp}^3 B_C}$	$\frac{4\tilde{\omega}_p^2 \Omega \epsilon v_{T\parallel} B}{\sqrt{\pi} \omega k_{\parallel} k_{\perp} v_{T\perp}^3 B_C}$	$\frac{4i\tilde{\omega}_p^2 v_{T\parallel} B^{3/2}}{\sqrt{\pi} \omega k_{\parallel} v_{T\perp}^2 B_C^{3/2}}$
$S_{l,n}$	1	n^2	n	ξ_n	n	1
$p_{l,0}$	$-\frac{B_C}{B} \frac{k_{\parallel} v_{T\parallel}}{\omega}$	$-\frac{B_C}{B} \frac{k_{\parallel} v_{T\parallel}}{\omega}$	$-\frac{B_C}{B} \frac{k_{\parallel} v_{T\parallel}}{\omega}$	η	η	η
$p_{l,1}$	$\frac{B_C}{B} \frac{k_{\parallel} v_{T\parallel}}{\omega} \frac{T_{\perp}}{T_{\parallel}}$	$\frac{B_C}{B} \frac{k_{\parallel} v_{T\parallel}}{\omega} \frac{T_{\perp}}{T_{\parallel}}$	$\frac{B_C}{B} \frac{k_{\parallel} v_{T\parallel}}{\omega} \frac{T_{\perp}}{T_{\parallel}}$	Λ	Λ	Λ
$q_{l,0}$	η	η	η	$\eta \xi_n$	$\eta \xi_n$	$\eta \xi_n$
$q_{l,1}$	Λ	Λ	Λ	$\Lambda \xi_n$	$\Lambda \xi_n$	$\Lambda \xi_n$
h_l	3	1	2	1	1	2

With $\eta = \frac{B_C}{B} \frac{n\epsilon\Omega}{\omega}$, $\Lambda = \frac{T_{\perp}}{T_{\parallel}} (1 - \eta)$. K_6, K_7 are not shown because they equal K_4, K_5 respectively. This can be seen by using the trick from Eq. (25) and dropping the odd integrand terms because $M(x), N(x)$ are even.

The most expensive part of the computation of $M(x), N(x)$ is calculating the Bessel functions J_n . However, the amount of evaluations can be minimised by using recurrence relations. Also symmetry properties can be used. For integer order n :

$$J_n(-z) = (-1)^n J_n(z), \quad J_{-n}(z) = (-1)^n J_n(z) \quad (\text{A.10})$$

And so:

$$J_{-n}^2(z) = J_n^2(z), \quad J_{-n}'^2(z) = J_n'^2(z), \quad J_{-n}(z)J_{-n}'(z) = J_n(z)J_n'(z) \quad (\text{A.11})$$

This means that no negative order Bessel functions need to be computed. The Fortran library for special functions [47] already takes care of this. It also computes the Bessel function derivatives in the same routine. In addition, significant time can in principle be saved by computing the Bessel functions once on a y grid, then reusing it for every x value. This however will not be accurate, as the $e^{-|x^2+by^2|}$ term in Eq. (A.9) becomes a narrow spike for $b < 0, x > 1$. Therefore it is more efficient to recompute the Bessel functions for every x value, on a new y grid with refinement around $y = x/\sqrt{|b|}$. Note, during this derivation it was assumed here that $\xi_n \in \mathbb{R}$, but k_{\perp} or λ can still be complex.

Appendix B. PIC coefficients

The coefficients for Eq. (27) in full:

$$\begin{aligned}
\tilde{\xi}_{n,j} &= \frac{\omega - n\epsilon\Omega - k_{\parallel}v_{\parallel,j}}{k_{\parallel}\sigma_j}, & b_j &= \frac{\epsilon k_{\perp}v_{\perp,j}}{\Omega} \\
c_{0,j} &= -2b_j \frac{v_{\perp,j}}{\sigma_j} \left(1 - \frac{k_{\parallel}v_{\parallel,j}}{\omega}\right) J_n(b_j) J'_n(b_j) \\
d_{0,j} &= 2b_j \frac{k_{\parallel}v_{\perp,j}}{\omega} J_n(b_j) J'_n(b_j) + 2 \frac{v_{\perp,j}^2}{\sigma_j^2} \frac{k_{\parallel}v_{\perp,j}}{\omega} \left[(J'_n(b_j))^2 - \frac{n^2}{b_j^2} J_n^2(b_j) \right] \\
c_{1,j} &= 2n^2 \frac{\epsilon\Omega}{k_{\perp}\sigma_j} \left(1 - \frac{k_{\parallel}v_{\parallel,j}}{\omega}\right) J_n(b_j) J'_n(b_j) \\
d_{1,j} &= -2n^2 \frac{\epsilon\Omega k_{\parallel}}{\omega k_{\perp}} J_n(b_j) J'_n(b_j) + 2n^2 \frac{\Omega^2 k_{\parallel}v_{\perp,j}}{\omega k_{\perp}^2 \sigma_j^2} J_n^2(b_j) \\
c_{2,j} &= in \frac{v_{\perp,j}}{\sigma_j} \left(1 - \frac{k_{\parallel}v_{\parallel,j}}{\omega}\right) \left[\left(\frac{n^2}{b_j^2} - 1\right) J_n^2(b_j) + (J'_n(b_j))^2 \right] \\
d_{2,j} &= -in \frac{k_{\parallel}v_{\perp,j}}{\omega} \left[\left(\frac{n^2}{b_j^2} - 1\right) J_n^2(b_j) + (J'_n(b_j))^2 \right] + 2in \frac{\epsilon\Omega k_{\parallel}v_{\perp,j}^2}{\omega k_{\perp} \sigma_j^2} J_n(b_j) J'_n(b_j) \\
c_{3,j} &= 2n \frac{k_{\perp}v_{\parallel,j}^2}{\omega\sigma_j} J_n(b_j) J'_n(b_j) \\
d_{3,j} &= 2 \frac{v_{\perp,j} (v_{\parallel,j} + \sigma_j \tilde{\xi}_{n,j})}{\sigma_j^2} \left(1 - \frac{\epsilon n\Omega}{\omega}\right) J_n^2(b_j) + 2n \frac{k_{\perp} (2v_{\parallel,j} + \sigma_j \tilde{\xi}_{n,j})}{\omega} J_n(b_j) J'_n(b_j) \\
c_{4,j} &= 2n^2 \frac{\epsilon\Omega v_{\parallel,j}}{\omega\sigma_j} J_n(b_j) J'_n(b_j) \\
d_{4,j} &= 2n^2 \frac{\epsilon\Omega}{\omega} J_n(b_j) J'_n(b_j) + 2n \frac{\epsilon\Omega v_{\perp,j}}{k_{\perp} \sigma_j^2} \left(1 - \frac{\epsilon n\Omega}{\omega}\right) J_n^2(b_j) \\
c_{5,j} &= in \frac{k_{\perp}v_{\parallel,j}v_{\perp,j}}{\omega\sigma_j} \left[\left(\frac{n^2}{b_j^2} - 1\right) J_n^2(b_j) + (J'_n(b_j))^2 \right] \\
d_{5,j} &= in \frac{k_{\perp}v_{\perp,j}}{\omega} \left[\left(\frac{n^2}{b_j^2} - 1\right) J_n^2(b_j) + (J'_n(b_j))^2 \right] + 2i \frac{v_{\perp,j}^2}{\sigma_j^2} \left(1 - \frac{\epsilon n\Omega}{\omega}\right) J_n(b_j) J'_n(b_j) \\
c_{6,j} &= 2n \frac{v_{\parallel,j}}{\sigma_j} \left(1 - \frac{k_{\parallel}v_{\parallel,j}}{\omega}\right) J_n(b_j) J'_n(b_j) \\
d_{6,j} &= 2n \left(1 - \frac{k_{\parallel}(2v_{\parallel,j} + \sigma_j \tilde{\xi}_{n,j})}{\omega}\right) J_n(b_j) J'_n(b_j) + 2n \frac{\epsilon\Omega k_{\parallel}v_{\perp,j}(v_{\parallel,j} + \sigma_j \tilde{\xi}_{n,j})}{\omega k_{\perp} \sigma_j^2} J_n^2(b_j) \\
c_{7,j} &= ib_j \frac{v_{\parallel,j}}{\sigma_j} \left(1 - \frac{k_{\parallel}v_{\parallel,j}}{\omega}\right) \left[\left(\frac{n^2}{b_j^2} - 1\right) J_n^2(b_j) + (J'_n(b_j))^2 \right] \\
d_{7,j} &= ib_j \left(1 - \frac{k_{\parallel}(2v_{\parallel,j} + \sigma_j \tilde{\xi}_{n,j})}{\omega}\right) \left[\left(\frac{n^2}{b_j^2} - 1\right) J_n^2(b_j) + (J'_n(b_j))^2 \right] \\
&+ 2i \frac{k_{\parallel}v_{\perp,j}^2 (v_{\parallel,j} + \sigma_j \tilde{\xi}_{n,j})}{\omega\sigma_j^2} J_n(b_j) J'_n(b_j)
\end{aligned} \tag{B.1}$$

The special case of $k_{\perp} = 0$ is handled separately by taking the limit of $k_{\perp} \rightarrow 0$ in Eq. (B.1). The second derivative of the Bessel function has been rewritten in terms of $J_n(z)$, $J'_n(z)$ as those are provided directly by the special functions library.

Appendix C. Plasma profiles

In the LEMan only simulations it was assumed that $T_i = T_e$, and the ion densities have the same profile shape as electrons, but scaled up by a given factor. For JET and W7-X the used profiles are shown in figure C1. For W7-X the electron profiles are estimates for what may be achieved in the second operational phase of W7-X: $N_e = N_{e,0}(0.9(1 - s^{10})^2 + 0.1)$, $N_{e,0} = 1.5 \cdot 10^{20} \text{m}^{-3}$, and $T_e = (3995(1 - s) + 5) \text{eV}$.

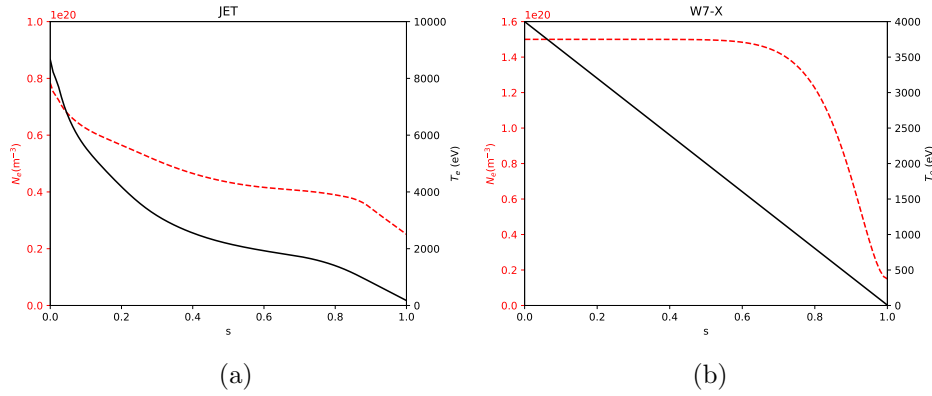


Figure C1: Plasma profiles used in the LEMan simulations. The left panel is for JET, the right is for W7-X. The left vertical axis corresponds to density, in red (dashed), and the right vertical corresponds to the temperature, in black (solid).

References

- [1] Stix T 1975 *Nuclear Fusion* **15** 737–754 ISSN 0029-5515 URL <https://iopscience.iop.org/article/10.1088/0029-5515/15/5/003>
- [2] Kiptily V, Cecil F, Jarvis O, Mantsinen M, Sharapov S, Bertalot L, Conroy S, Ingesson L, Johnson T, Lawson K, Popovichev S and contributors to the EFDA-JET Workprogramme 2002 *Nuclear Fusion* **42** 999–1007 URL <https://doi.org/10.1088/0029-5515/42/8/308>
- [3] Mayoral M L, Lamalle P, Eester D V, Lerche E, Beaumont P, Luna E D L, Vries P D, Gowers C, Felton R, Harling J, Kiptily V, Lawson K, Laxback M, Lomas P, Mantsinen M, Meo F, Noterdaeme J M, Nunes I, Piazza G, Santala M and contributors J E 2006 *Nuclear Fusion* **46** S550–S563 URL <https://doi.org/10.1088/0029-5515/46/7/S14>
- [4] Saito K, Kumazawa R, Seki T, Kasahara H, Osakabe M, Isobe M, Shimpō F, Nomura G, Watari T, Murakami S, Sasao M, Mutoh T and Group L E 2010 *Fusion Science and Technology* **58** 515–523 (Preprint <https://doi.org/10.13182/FST10-A10838>) URL <https://doi.org/10.13182/FST10-A10838>
- [5] Graves J P, Hopcraft K I, Dendy R O, Hastie R J, McClements K G and Mantsinen M 2000 *Phys. Rev. Lett.* **84**(6) 1204–1207 URL <https://link.aps.org/doi/10.1103/PhysRevLett.84.1204>
- [6] Jucker M, Graves J P, Cooper G A and Cooper W A 2008 *Plasma Physics and Controlled Fusion* **50** 065009 URL <https://doi.org/10.1088/0741-3335/50/6/065009>

- [7] Mantsinen M J, Eriksson L G, Gauthier E, Hoang G T, Joffrin E, Koch R, Litaudon X, Lyssoivan A, Mantica P, Nave M F F, Noterdaeme J M, Petty C C, Sauter O and Sharapov S E 2003 *Plasma Physics and Controlled Fusion* **45** A445–A456 URL <https://doi.org/10.1088/0741-3335/45/12a/028>
- [8] Sharapov S, Hellsten T, Kiptily V, Craciunescu T, Eriksson J, Fitzgerald M, Girardo J B, Goloborod'ko V, Hellesen C, Hjalmarsson A *et al.* 2016 *Nuclear Fusion* **56** 112021 URL <https://doi.org/10.1088/0029-5515/56/11/112021>
- [9] Hedin J 2001 *Ion cyclotron resonance heating in toroidal plasmas* Ph.D. thesis Alfvénlaboratoriet
- [10] Jaeger E F, Berry L A, Ahern S D, Barrett R F, Batchelor D B, Carter M D, D'Azevedo E F, Moore R D, Harvey R W, Myra J R, D'Ippolito D A, Dumont R J, Phillips C K, Okuda H, Smithe D N, Bonoli P T, Wright J C and Choi M 2006 *Physics of Plasmas* **13** 056101 (*Preprint* <https://doi.org/10.1063/1.2173629>) URL <https://doi.org/10.1063/1.2173629>
- [11] Lerche E, Van Eester D, Krasilnikov A and Lamalle P 2007 *AIP Conference Proceedings* **933** 51–54 (*Preprint* <https://aip.scitation.org/doi/pdf/10.1063/1.2800547>) URL <https://aip.scitation.org/doi/abs/10.1063/1.2800547>
- [12] Bilato R, Brambilla M, Maj O, Horton L, Maggi C and Stober J 2011 *Nuclear Fusion* **51** 103034 URL <https://doi.org/10.1088/0029-5515/51/10/103034>
- [13] Jucker M 2010 *Self-consistent ICRH distribution functions and equilibria in magnetically confined plasmas* Ph.D. thesis EPFL
- [14] Patten H W 2019 *Development and optimisation of advanced auxiliary ion heating schemes for 3D fusion plasma devices* Ph.D. thesis EPFL
- [15] Dendy R O, Hastie R J, McClements K G and Martin T J 1995 *Physics of Plasmas* **2** 1623–1636 (*Preprint* <https://doi.org/10.1063/1.871457>) URL <https://doi.org/10.1063/1.871457>
- [16] Casson F, Patten H, Bourdelle C, Breton S, Citrin J, Koechl F, Sertoli M, Angioni C, Baranov Y, Bilato R, Belli E, Challis C, Corrigan G, Czarnecka A, Ficker O, Frassinetti L, Garzotti L, Goniche M, Graves J, Johnson T, Kirov K, Knight P, Lerche E, Mantsinen M, Mylnar J and *et al.* 2020 *Nuclear Fusion* **60** 066029 URL <https://doi.org/10.1088/1741-4326/ab833f>
- [17] Cooper W, Hirshman S, Merkel P, Graves J, Kisslinger J, Wobig H, Narushima Y, Okamura S and Watanabe K 2009 *Computer Physics Communications* **180** 1524 – 1533 ISSN 0010-4655 URL <http://www.sciencedirect.com/science/article/pii/S0010465509001179>
- [18] Pfefferlé D, Cooper W, Graves J and Misev C 2014 *Computer Physics Communications* **185** 3127 – 3140 ISSN 0010-4655 URL <http://www.sciencedirect.com/science/article/pii/S0010465514002744>
- [19] Hellsten T, Johnson T, Carlsson J, Eriksson L G, Hedin J, Laxåback M and Mantsinen M 2004 *Nuclear Fusion* **44** 892–908 URL <https://doi.org/10.1088/0029-5515/44/8/008>
- [20] Jaeger E F, Berry L A and Batchelor D B 2000 *Physics of Plasmas* **7** 3319–3329 (*Preprint* <https://doi.org/10.1063/1.874197>) URL <https://doi.org/10.1063/1.874197>
- [21] Brambilla M 1999 *Plasma Physics and Controlled Fusion* **41** 1–34 URL <https://doi.org/10.1088/0741-3335/41/1/002>
- [22] Brambilla M and Bilato R 2009 *Nuclear Fusion* **49** 085004 URL <https://doi.org/10.1088/0029-5515/49/8/085004>
- [23] Dumont R 2009 *Nuclear Fusion* **49** 075033 URL <https://doi.org/10.1088/0029-5515/49/7/075033>
- [24] Joly J, Garcia J, Imbeaux F, Dumont R, Schneider M, Johnson T and Artaud J F 2019 *Plasma Physics and Controlled Fusion* **61** 075017 URL <https://doi.org/10.1088/1361-6587/ab1f54>
- [25] Lamalle P 1994 *Nonlocal theoretical generalization and tridimensional numerical study of the coupling of an ICRH antenna to a tokamak plasma* Ph.D. thesis LPP - ERM/KMS
- [26] Lamalle P U 1997 *Plasma Physics and Controlled Fusion* **39** 1409–1460 URL <https://doi.org/10.1088/0741-3335/39/9/011>
- [27] VAN EESTER D 2001 *Journal of Plasma Physics* **65** 407–452
- [28] Villard L, Appert K, Gruber R and Vaclavik J 1986 *Computer Physics Reports* **4** 95–135 ISSN 0167-7977 URL <https://www.sciencedirect.com/science/article/pii/0167797786900274>

- [29] Laxåback M 2005 *Fast wave heating and current drive in tokamaks* Ph.D. thesis KTH
- [30] Stix T H 1992 *Waves in plasmas* (Springer Science & Business Media)
- [31] Brambilla M 1998 *Kinetic theory of plasma waves: homogeneous plasmas* 96 (Oxford University Press)
- [32] Swanson D G 2003 *Plasma waves (2nd edition)* (IOP Publishing)
- [33] nan Jiang B, Wu J and Povinelli L 1996 *Journal of Computational Physics* **125** 104–123 ISSN 0021-9991 URL <https://www.sciencedirect.com/science/article/pii/S0021999196900820>
- [34] Jaeger E, Batchelor D, Carter M and Weitzner H 1990 *Nuclear Fusion* **30** 505–519 URL <https://doi.org/10.1088/0029-5515/30/3/012>
- [35] Jaun A, Appert K, Vaclavik J and Villard L 1995 *Computer Physics Communications* **92** 153–187 ISSN 0010-4655 URL <https://www.sciencedirect.com/science/article/pii/0010465595001056>
- [36] Popovich P, Cooper W and Villard L 2006 *Computer Physics Communications* **175** 250–263 ISSN 0010-4655 URL <https://www.sciencedirect.com/science/article/pii/S0010465506001457>
- [37] Cooper W, Graves J, Hirshman S, Yamaguchi T, Narushima Y, Okamura S, Sakakibara S, Suzuki C, Watanabe K, Yamada H and Yamazaki K 2006 *Nuclear Fusion* **46** 683–698 URL <https://doi.org/10.1088/0029-5515/46/7/001>
- [38] Kerbel G D and McCoy M G 1985 *The Physics of Fluids* **28** 3629–3653 (*Preprint* <https://aip.scitation.org/doi/pdf/10.1063/1.865319>) URL <https://aip.scitation.org/doi/abs/10.1063/1.865319>
- [39] Harvey R, McCoy M, Kerbel G and Chiu S 1986 *Nuclear fusion* **26** 43
- [40] Chang C S and Colestock P 1990 *Physics of Fluids B: Plasma Physics* **2** 310–317 ISSN 0899-8221 URL <http://aip.scitation.org/doi/10.1063/1.859319>
- [41] Faustin J M P 2017 *Self-consistent interaction of fast particles and ICRF waves in 3D applications of fusion plasma devices* Ph.D. thesis
- [42] Kazakov Y, Eester D V, Dumont R and Ongena J 2015 *Nuclear Fusion* **55** 032001 URL <https://doi.org/10.1088/0029-5515/55/3/032001>
- [43] Hirshman S P and Whitson J C 1983 *The Physics of Fluids* **26** 3553–3568 (*Preprint* <https://aip.scitation.org/doi/pdf/10.1063/1.864116>) URL <https://aip.scitation.org/doi/abs/10.1063/1.864116>
- [44] Jaeger E F, Berry L A, D’Azevedo E, Batchelor D B, Carter M D, White K F and Weitzner H 2002 *Physics of Plasmas* **9** 1873–1881 (*Preprint* <https://doi.org/10.1063/1.1455001>) URL <https://doi.org/10.1063/1.1455001>
- [45] Lamalle P, Mantsinen M, Noterdaeme J M, Alper B, Beaumont P, Bertalot L, Blackman T, Bobkov V, Bonheure G, Brzozowski J, Castaldo C, Conroy S, de Baar M, de la Luna E, de Vries P, Durodié F, Ericsson G, Eriksson L G, Gowers C, Felton R, Heikkinen J, Hellsten T, Kiptily V, Lawson K, Laxåback M, Lerche E, Lomas P, Lyssoivan A, Mayoral M L, Meo F, Mironov M, Monakhov I, Nunes I, Piazza G, Popovichev S, Salmi A, Santala M, Sharapov S, Tala T, Tardocchi M, Eester D V, Weyssow B and contributors J E 2006 *Nuclear Fusion* **46** 391–400 URL <https://doi.org/10.1088/0029-5515/46/2/021>
- [46] Fried B D and Conte S D 1961 *The plasma dispersion function: the Hilbert transform of the Gaussian* (Academic Press)
- [47] Shanjie Zhang J J 1996 *Computation of Special Functions* (Wiley) ISBN 0-471-11963-6